International Journal of Innovation and Applied Studies
ISSN 2028-9324 Vol. 43 No. 3 Sep. 2024, pp. 859-881

http://www.ijias.issr-journals.org/

# Evaluation of conductive energy flux within cultivated land based on biophysical parameters: A case study in the Yamoussoukro area

***Sahi Roland Diomande, Yao N'Guessan, and Kotchi Rémi N'Guessan***

Laboratoire de Mécanique et Sciences des Matériaux, Institut National Polytechnique Félix Houphouët-Boigny (INP-HB), BP 1093 Yamoussoukro, Côte d'Ivoire



**ABSTRACT:** With global warming, heat stress is a phenomenon that is having a major impact on agricultural production. The extreme amounts of conductive heat during periods of drought to which soil surfaces and plants are subjected produce heat stress in crops. To predict these extreme conditions and anticipate actions to adapt our staple crops, an assessment of the energy potential within soils based on long-term hygrothermal behaviour has been carried out. This document assesses the conductive energy flux penetrating cultivated land in the Yamoussoukro area, based on biophysical properties, with the aim of controlling average seasonal and annual changes in energy fluxes. The study considered the closed energy balance model and modified it to obtain an estimate of heat fluxes in real time and space. The results showed that the Yamoussoukro area has two dry seasons contrasted by two rainy seasons with decreasing rainfall since 2013. High amounts of conductive energy were obtained between November and April, and between August and September, varying between -50 W/m$^2$ and -25 W/m², while they were high (0 to 50 W/m²) in the rainy seasons. The calculated average annual net radiant heat flux, latent heat flux, sensible heat flux and conductive heat flux are 221.405 W/m², 218.592 W/m², 44.290 W/m² and -22.270 W/m², respectively. The lightness indices varied from 0.26 to 0.7, while the leaf area indices of the cocoa leaves varied from 2 to 5.42 m²/m².

**KEYWORDS:** Net radiant heat flux, latent heat flux, sensible heat flux, conductive heat flux, biophysical parameters, cultivated land.

## 1 INTRODUCTION

As climate change warms the planet's surface, crops are being exposed to excessive amounts of thermal energy [1]. This is because cultivated land is a heterogeneous environment whose surfaces are exposed to the effects of direct and indirect solar radiation [2]. During the day, solar radiation heats the earth's surface. Except for energy losses through turbulence, some of the sun's energy is transmitted by radiation to the earth's surface and penetrates the soil to give life to the environment (plants, microorganisms, etc.). Heat within the soil is an inseparable component of the energy balance at the earth's surface. This heat is important in the energy balance generated by the earth's surface during periods when solar radiation is unavailable [3]. For this reason, knowledge of the energy balance within soils is of interest to several fields of application [3, 4] including agriculture, civil engineering, bioenergy, communication networks, biology, meteorology, hydrogeology, etc. [5, 6].

The energy balance of soils consists mainly of heat fluxes from net solar radiation, latent heat fluxes and sensible heat fluxes producing a conductive heat flux in the soil [4]. Consequently, the resulting conductive heat flux plays a crucial role in the variation of environmental hydrothermal properties and plant development. This is made possible by thermo-hydric exchanges in the soil-plant-atmosphere system. Heat propagation in soils is essentially by conduction [2]. In the absence of the necessary plant cover, the intensity of conductive energy within the soil is sometimes significant and can exceed the needs of the plants. A large amount of this conductive energy acts on plant roots, causing heat stress to crops [7].

To cushion the effects of excessive heat, accurate prediction of the conductive energy flux of cultivated land will enable crops to be grown that are adapted to the soil and climate, thereby increasing crop productivity. In fact, this practice will enable plants to withstand bad weather. Plant cover therefore plays a vital role in the heat and water exchange between the soil-

**Corresponding Author:** Sahi Roland Diomande 

plant-atmosphere system [8]. Unfortunately, the exact estimation of the conductive energy flux in the soil layers necessary for plant development is often difficult because of the study assumptions made, which leave out certain important biophysical parameters.

Several models have been developed in the past to estimate the heat flux within soils. These models fall into two broad categories: models based on direct measurements of soil heat flux and models based on indirect methods. Direct methods involve estimating soil heat from the temperature gradient using multi-layer [8, 9, 10] or single layer [11] observation data, and models based on the integration of soil heat fluxes requiring temperature and moisture measurements in deep soils [12]. Indirect techniques are based either on the ratio of heat stored in the soil at a reference depth where the heat is measured by plates, or are derived from the gradient method [13], or on the residual of the energy balance equation [14, 15], or on the propagation of heat in sinusoidal or harmonic form, or on Fourier's law [13, 16].

However, most of the direct and indirect models that escape the closed energy balance [9, 17, 18, 19, 20], generate significant calculation errors and do not provide an optimal representation [21, 22]. Previous techniques for estimating soil energy fluxes are confronted with energy imbalance problems related to the estimation scale, soil surface heterogeneity and turbulent fluxes [18, 23]. These problems influence the calibration and validation of these models [16, 24]. Measurement errors, corrections and heat flux fingerprints have attracted a great deal of scientific attention [18, 19, 24, 25, 26, 27]. This observation makes the present study an evaluation of thermal potentials based on the principle of closed energy balance.

In addition, as weather conditions and soil surface heterogeneity change, energy and moisture exchanges between the soil surface and its surrounding environment are affected [28]. The main exchanges of heat and water vapour that drive global and local weather conditions between the earth's surface and the atmosphere are mainly via turbulent and diffusive fluxes in the earth's surface layers. Many weather and climate phenomena are therefore influenced by processes associated with land-atmosphere interactions, in which soil moisture and its control through evapotranspiration play a major role [29]. The projection of reliable regional climate parameters requires the establishment of improved models of the soil-plant-atmosphere system. In indirect methods, the exchanges between the soil surface and its feedback processes with the atmosphere, under different climatic regimes for land properties and land use, must be represented [28]. In establishing models of conductive energy flux into or out of soils, albedo [30] plant properties and environmental parameters must be taken into account along with the role of vegetation.

The aim of this article is to assess the conductive energy flux of cultivated land based on meteorological and biophysical data. Specifically, the overall objective has been divided into three parts: i) Assessment of average hygrothermal parameters in the Yamoussoukro area from 2011 to 2021; ii) Estimation of energy fluxes within croplands from biophysical parameters; iii) Establishment of the relationship between turbulent energy fluxes and available energy fluxes.

## 2 MATERIALS AND METHODS

### 2.1 MATERIALS

#### 2.1.1 PRESENTATION OF THE STUDY AREA

The study site is a cocoa field located in the village of Ménou, belonging to the department of Yamoussoukro, situated between latitudes 6°20'N and 7°00"N and longitudes 4°40'W and 5°30"W with an area of 478938 km$^2$ [31], in central Côte d'Ivoire. This 320m×960m field has been used exclusively for growing dated cocoa for more than 15 years. The site is subject to a humid tropical climate with forest vegetation [32] consisting of mesophilous forest, gallery forest and shrubby Savannah, as well as two rainy seasons, with mean annual rainfall and temperature of 1148 mm/year and 26.39°C, respectively [33]. The Yamoussoukro area is not very hilly and is marked by wooded Savannah plateaux. The geomorphological landscape of this area is characterised by pediplains with quasi-rectilinear slopes, flat lowlands and flattened, low granite mountain ranges with an average altitude of 200 m [31, 32]. The soils studied are moderately humified ferralitic with sandy-clay textures on granitic and sedimentary rocks, which are the most abundant in this department. [35]. The volumetric moisture content of the saturated soil, the field capacity and the wilting point are 0,641 m$^3$/ m$^3$, 0,435 m$^3$/ m$^3$ and 0,201 m$^3$/ m$^3$ respectively.

#### 2.1.2 METEOROLOGICAL DATA

Weather forecasting in an area requires decadal data [36]. This study used meteorological data recorded in 1-minute steps over 11 years (2011 to 2021) by the Vantage Pro2 station installed at INP-HB (Ivory Coast). The station consists of two main components: outdoor sensors (ISS) version 6152EU and a reception console. The ISS measures outdoor temperature, outdoor

relative humidity, global irradiation, precipitation, wind speed and direction. Temperature and relative humidity were measured using a digital sensor placed in a standardised, naturally ventilated shelter. Rainfall is measured using a double tilting trough (when a trough is full, the system tilts and the console counts 0.225 mm of rain) and the troughs are emptied automatically. The anemometer/wind vane can be detached from the ISS to measure wind speed and direction, and is fitted with a 12 m cable. Among the data measured, ambient temperature, relative humidity, precipitation, global irradiation and wind speed were used as input parameters for the model. Each data unit contained 95040 values (24 hours X 30 days X 12 months X 11 years), making a database of 475200 values.

### 2.2 METHODS

#### 2.2.1 EVALUATION OF AVERAGE HYGROTHERMAL PARAMETERS IN THE YAMOUSSOUKRO AREA (2011–2021)

The meteorological data was processed and analysed, and the average daily, monthly and annual values were used as input parameters for the model. The meteorological database was analysed using Microsoft Excel software, which enabled temporal variations in the environmental parameters considered to be observed. The estimation of solar and rainfall potentials made it possible to determine the average daily, monthly and annual variations in global solar irradiation, the brightness index, rainfall and relative air humidity in the Yamoussoukro area.

The clearness index ($K_t$) indicates the degree of reduction in global solar radiation incident by the sky, providing information on the transparency of the atmosphere in a given area [37]. This index corresponds to the ratio between the intensity of global solar radiation and the intensity of extraterrestrial solar radiation [38] :

$$K_t = \frac{G}{R_a} \text{ [Eq. 1]}$$

$G$ : average global solar radiation intensity (W/m²) ; $R_a$ : extraterrestrial solar radiation (W/m²).

The extraterrestrial solar radiation intensity of a surface reflects its capacity to receive solar radiation outside the atmosphere. This energy potential is invariant from one year to the next, but depends only on the number of days in the year, the coordinates of the sun and the geography of the site under consideration. It is expressed as follows [39] :

$$R_a = 37.6.\, d_r[\omega_c\, sin(\varphi)\, sin(\delta) + cos(\varphi)\, cos(\delta)\, sin(\omega_c)] \text{ [Eq. 2]}$$

$d_r$ *:* earth-sun distance*,* $\omega_C$ *:* hour angle at sunset*,* $\Phi$ *:* latitude of location (radian) ; $\delta$ *:* declination of location (radian).

The distance from the earth to the sun is calculated by the equation:

$$d_r = 1 + 0.033.\, cos\left[\frac{2\pi}{365} * n_j\right] \text{ [Eq. 3]}$$

$n_j$ : number of day j in the year.

#### 2.2.2 ESTIMATION OF ENERGY FLUXES WITHIN CULTIVATED LAND BASED ON BIOPHYSICAL PARAMETERS

##### 2.2.2.1 NET ENERGY BALANCE EQUATION AT GROUND SURFACE

Accurate assessment of energy fluxes at the earth's surface requires the energy balance equation to be closed [24, 37, 38, 39]. The energy balance equation at the earth's surface governs the periodic variation of net solar radiation, sensible heat flux, latent heat flux and conductive heat flux [43]. Neglecting the effects of photosynthesis and the amount of energy stored in soils due to their low intensities, the net energy balance equation at the earth's surface is given [2, 3] :

$$R_{net} = G_0 + (H + \lambda E) \text{ [Eq. 4]}$$

$G_0$ **:** flux of heat by conduction in the soil at time $t$ and depth $z_j$ *(W.m$^{-2}$) ;* $H$ *:* flux of sensible heat or heat by convection at the soil surface at time $t$ *(W.m$^{-2}$) ;* $\lambda E$ *:* flux of latent heat or evapotranspiration at time $t$ (W.m$^{-2}$).

#### 2.2.2.1.1 STUDY HYPOTHESES

The relationships between the components of the soil-plant-atmosphere system have been established on the basis of the following assumptions:

- Heat fluxes through net solar radiation and convection are the main sources of energy for soils and plants;
- Heat exchanges within the soil take place vertically in both directions (downwards by conduction and upwards by evaporation) ;
- The spatio-temporal characteristics of a layer of soil and ambient air measured/calculated at a given depth/height for a given time are constant;
- Plants in the same plot have the same average size (average canopy height), leaf resistance and leaf temperature;
- Cultivated land has a constant rate of plant cover.

#### 2.2.2.1.2 NET SOLAR RADIATION INTENSITY

Net solar radiation represents the proportion of global solar radiation that reaches the ground surface directly or indirectly. The variation in net solar radiation intensities is expressed by the Stefan-Boltzmann law [45] :

$$R_{net} = (1 - \alpha).R_{swd} + \varepsilon.\sigma\left(\varepsilon_a {T_{am}}^4 - {T_s}^4\right) \text{ [Eq. 5]}$$

$\varepsilon$ : ground surface emissivity; $\sigma$ : Stefan-Boltzmann constant (5.67. $10^{-8}$ W/m².°K$^{-4}$) ; $\varepsilon_a$ : effective emissivity of the atmosphere; $T_{am}$ : ambient air temperature; $T_s$ : soil surface temperature measured at a depth of 8cm; $R_{swd}$ : downward solar radiation; $\alpha$ : albedo of the ground surface. The albedo of a natural dual surface covered with vegetation is 0.25 compared with a value of 0.13 for bare ground surfaces [46].

The downward radiation is given by the formula [47] :

$$R_{swd} = \left(a_S - b_S \frac{n_i}{N}\right) W_d \text{ [Eq. 6]}$$

$a_S = 0.2$ and $b_S = 0.5$ : values of empirical regression coefficients recommended in the literature [48] ; $n_i$: actual daily sunshine duration; N : maximum daily sunshine duration; $\frac{n_i}{N}$ : relative sunshine duration ($n\_i/N \in [0\ ;\ 1]$) ; $W\_d$ : daily astronomical radiation (W.m$^{-2}$).

The maximum sunshine duration is expressed by the relationship [49] :

$$N = \frac{24}{\pi}.ar\,cos(-tan(\varphi).tan(\delta)) \text{ [Eq. 7]}$$

The actual daily sunshine duration was obtained by counting the hours during which the intensity of global solar irradiation is non-zero.

The declination was calculated using the expression [49] :

$$\delta = 23.45.sin\left((2\pi(n\_j + 284)/365\right) \text{ [Eq. 8]}$$

The daily astronomical radiation intensity is calculated using the relationship :

$$W_d = \frac{N}{2.\pi} K_D.I_0.[\omega_0.sin(\phi).sin(\delta) + cos(\phi).sin(\omega_0)] \text{ [Eq. 9]}$$

$K_D$ : correction coefficient for the Earth-Sun distance or correction factor for the eccentricity of the Earth's orbit; $I_0$ : solar constant $\left(1657 \frac{W}{m^2}\right)$ ; $\omega_C$: hourly angle.

The Earth-Sun distance correction coefficient is a function of the number of days in the year and is evaluated by:

$$K_D = 1 - 0.034.sin\left(\frac{2.\pi(n_j - 94)}{180}\right) \text{ [Eq. 10]}$$

The hour angle at sunrise is calculated by the relationship :

$$\omega_L = arcos\big(-tan(\varphi)\,.\,tan[\![(\delta)]\!]\big)$$ [Eq. 11]

The expression for the hour angle at sunset ($\omega_C$) is the opposite of that at sunrise. In fact, $\omega_L = \omega_0$ at sunrise and $\omega_C = -\omega_0$, at sunset. The hour angle ($\omega_0$) is counted positive in the afternoon and corresponds to $\omega_c$ while its values are negative pre-morning, corresponding to $\omega_L$.

The emissivity of the earth's surface is represented by the relationship:

$$\varepsilon = \varepsilon_V . f_C(\xi) + \varepsilon_g . f_S(\xi) + 4.\Delta\varepsilon . f_S(\xi)$$ [Eq. 12]

$f_C(\xi)$ : fraction of vegetation cover where $\xi$ is the correction angle of the fraction of vegetation cover or the observation angle; $f_S(\xi)$: fraction of uncovered soil surface; $\Delta\varepsilon$ : model tolerance ($\Delta\varepsilon \in [0\ ;\ 0.02]$) ; $\varepsilon_V$ : emissivity of a soil surface completely covered by vegetation in the spectral region between 10.5 µm and 12.5 µm ($\varepsilon_V = 0.985 \pm 0.007$); $\varepsilon_g$ : emissivity of a bare soil surface in the spectral region between 10.5 µm and 12.5 µm $(\varepsilon_g = 0.96 \pm 0.01)$. The value of the emissivity of the earth's surface calculated in this study is 0.986.

The vegetation cover fraction is defined as the vertical projection of the surface proportion of the landscape occupied by green vegetation [50]. The vegetation cover fraction is a function of the leaf area index (LAI) of the plants and is represented as follows:

$$f_C(\xi) = 1 - exp\left(\frac{-0.5*LAI}{cos(\xi)}\right)$$ [Eq. 13]

To determine the leaf area index, the LAI MOD15A2 version 2021 product was used per season with an applied spatial resolution of 500 m at a height of 10 m. The link to the MOD15A2 LAI product is as follows (http://eospso.gsfc.nasa.gov ) [51]. The MODIS product has been widely used and provides accurate resolution [42, 47, 49]. The value of the canopy fraction correction angle ($\xi$) simulated in this study is 5°. This correction angle is the angular value that maximises the fraction of the uncovered soil surface, while it minimises that of the vegetation cover. The fraction of the soil surface not covered by plant leaves is calculated by the relationship [50] :

$$f_S(\xi) = 1 - f_C(\xi)$$ [Eq.14]

The effective emissivity of the atmosphere is given by equation:

$$\varepsilon_a = 1.24\left(\frac{e_a}{T_{am}+273.16}\right)^{1/7}$$ [Eq. 14]

$e_a$ : air vapour pressure at the reference surface (kPa).

The air vapour pressure at the reference surface is given by the expression [29] :

$$e_a = 0.6108.\,exp\left(\frac{17{,}27}{T_{am}+237.3}\right)\left(\frac{RH_a}{100}\right)$$ [Eq. 15]

$RH_a$ : relative humidity of the ambient air (%).

#### 2.2.2.1.3 Evaluation Of Sensible Heat Flux

##### 2.2.2.1.3.1 Modification Of The Surface Energy Balance System (SEBS) Model

The Surface Energy Balance System model is used to evaluate the evaporative fraction of the soil and the transpiring fraction of the plant surface. Based on equations from previous studies, the sensible heat flux and evaporative heat flux equations have been transformed to give an improved expression. This new model makes up for the deficiencies in the complexity of previous SEBS models. A ground surface covered by vegetation subject to the seasonal effects of environmental parameters (wind speed, rain, sunshine, etc.) is subject to sensible heat flux. Vidal [47] has highlighted the influence of aerodynamic resistance ($r_{ae}$) and soil resistance ($r_{soil}$) on variations in sensible heat flux. However, this author and previous studies did not take into

account the influence of stomatal resistance of plant leaves on sensible heat flux. The introduction of plant leaf resistance is of interest insofar as plant leaves are part of the shading sources of irradiation profiles at the soil surface. In the present study, the impact of resistances (stomatal resistance of plant leaves, soil resistance, aerodynamic resistance (for the layer above the canopy) and air resistance ($r_{am}$) (for the layer below the canopy) ) on the variation in sensible heat flux was taken into account. The modified form of the sensible heat flux equation is written:

$$H = k.\mu.\frac{\rho_{air}.C_{P,air}}{r_{soil}+r_a+r_{leaves}}.(T_s - T_{am}).\left[ln\left(\frac{z-d_0}{z_{0h}}\right)\underbrace{-\Psi_h\left(\frac{z-d_0}{L}\right)+\Psi_h\left(\frac{z_{0h}}{L}\right)}_{a}\right]^{-1} \quad \text{[Eq. 17]}$$

$r_{leaves}$: stomatal resistance of collected leaves (s/m) ; $r_{soil}$ : vapour diffusion resistance of the soil (s/m) ; $r_a$ : equivalent air resistance between the aerodynamic resistance at the reference surface, calculated at 10 metres ($r_{ae}$) (s/m), and the resistance of the layer of air below the canopy ($r_{am}$), calculated at 2 metres from the ground surface.; $C_{P,air}$ : specific heat of the air (J/kg) ; $\Psi_h$*:* correction function for sensible heat stability, L : Obukhov's length; $\rho_{air} = \frac{0.34838*P_{atm}}{T_a+273,15}$ : density of the ambient air (kg.m$^{-3}$) ; $P_{atm}$ : measured atmospheric pressure (kPa) ; *z* : height at which wind speed is measured, expressed as $z = z_h + 2$ (m), ($z_h$ is the average height of the canopy (m) ) ; $d_0 = \frac{2}{3}.z_h$ : height of the zero displacement plane (m) ; $k = 0.46$ : Von Kármán constant; $z_{0h}$: length of thermal roughness (m) ; $T_a$: average of ambient temperatures measured at 2 metres ($T_{am}$) and 10 metres ($T_{ae}$).

The stomatal resistance of leaves depends on the turgidity of the guard cells. This resistance is controlled by solar radiation, rainfall, relative humidity of the ambient air, wind speed, soil type and the density of the leaves themselves [53] The stomatal resistance of the leaves was measured during the day and at night using an SC-1 porometer [54]. The average value of this resistance is 300 s/m, for several leaves collected in dry and rainy seasons, was used.

The underlined term in equation (Eq.17), is calculated from the wind speed measured at height z and the ratio between the length of mechanical roughness ($z_{0m}$) and the length of thermal roughness ($z_{0h}$) [44] :

$$\left(\frac{\mu}{\mu_*}\right).k = \left[ln\left(\frac{z-d_0}{z_{0m}}\right) - \Psi_m\left(\frac{z-d_0}{L}\right)+\Psi_m\left(\frac{z_{0m}}{L}\right)\right] \text{[Eq. 18]}$$

$\Psi_m$*:* Stability correction function for momentum transfer; $z_{0m}$ : mechanical roughness length for momentum at the earth's surface *($z_{0m} = 0{,}13.z_h$) ; $\mu$ :* wind speed measured at reference height at 2 metres (m/s) ; $\mu_*$ *:* friction velocity (m/s).

The stability correction function for momentum transfer is expressed as follows:

$$-\Psi_m\left(\frac{z-d_0}{L}\right)+\Psi_m\left(\frac{z_{0m}}{L}\right) = \left(\frac{\mu}{\mu_*}\right).k - ln\left(\frac{z-d_0}{z_{0m}}\right) \text{[Eq. 19]}$$

This expression originates from the work of SU in 2002 [55] and was improved by Hamimed *et al.*, in 2018 [56]. The latter relied on similarity theory using the parameter $k.B^{-1}$ to relate the thermal roughness length to the mechanical roughness length as follows [55] :

$$\frac{z_{0m}}{z_{0h}} = \frac{1}{\exp(kB^{-1})} \text{[Eq. 20]}$$

$kB^{-1}$*:* characteristic parameter of the model.

#### 2.2.2.1.3.2 RELATIONSHIP BETWEEN THERMAL ROUGHNESS LENGTH AND MECHANICAL ROUGHNESS LENGTH

From Figure 1, it was assumed that the relationship [Eq.20] is only valid for characterising the density of the plant layer (thickness of the intermediate layer) because this layer balances the thermomechanical properties in the ambient air ($\Psi\_h = \Psi\_m$). For a better estimate of the sensible heat in the air layer below the thickness of the plant leaves and the sensible heat produced above the plant surface, the above relationship is no longer appropriate. A new relationship based on a proportionality coefficient was established. This new relationship considered that the variations in the quantities of heat and motion (thermal properties and environmental mechanical properties are different ($\Psi\_m \neq \Psi\_h$)). In this relationship, the thermal properties (thermal roughness length and stability correction function for sensible heat) and mechanical properties

(mechanical roughness length and stability correction function for momentum transfer) are linked by a proportionality coefficient K according to the relationship:

$$\frac{z_{0m}}{z_{0h}} = \frac{1}{\exp(kB^{-1})} * K \text{ [Eq. 21]}$$

Such as $K = k'.\frac{-\Psi_m\left(\frac{z-d_0}{L}\right)+\Psi_m\left(\frac{z_{0m}}{L}\right)}{-\Psi_h\left(\frac{z-d_0}{L}\right)+\Psi_h\left(\frac{z_{0h}}{L}\right)}$

The purpose of the proportionality coefficient is to take into account the reduction in heat flux as it reaches the ground surface after passing through obstacles caused by the layers of plant leaves and environmental factors. The parameters of the momentum stability function such as aerodynamic resistance, the ambient temperature ($T_{ae}$) and mechanical roughness length were measured above the average canopy surface while those of the sensible heat transfer stability function, the ambient temperature ($T_{am}$), soil surface temperature and soil resistance were measured below the lower leaf boundary layer. The intermediate layer characterises shading (a layer resistant to thermal and mechanical diffusion). The intermediate layer minimises the intensity of heat transfer by radiation, convection and conduction. According to SU *et al.,* (2019) [57], the study of the energy balance at the earth's surface consists of decomposing the cultivated domain into three vertical layers (surface below the leaves, density layer of the leaves and layer above the canopy) by considering the sensible heat fluxes and long-wave radiations in the tree canopy, the forest airspace and the soil surface layers of forest ecosystems. Figure 1 summarises the different levels of measurement of the model's characteristic parameters.

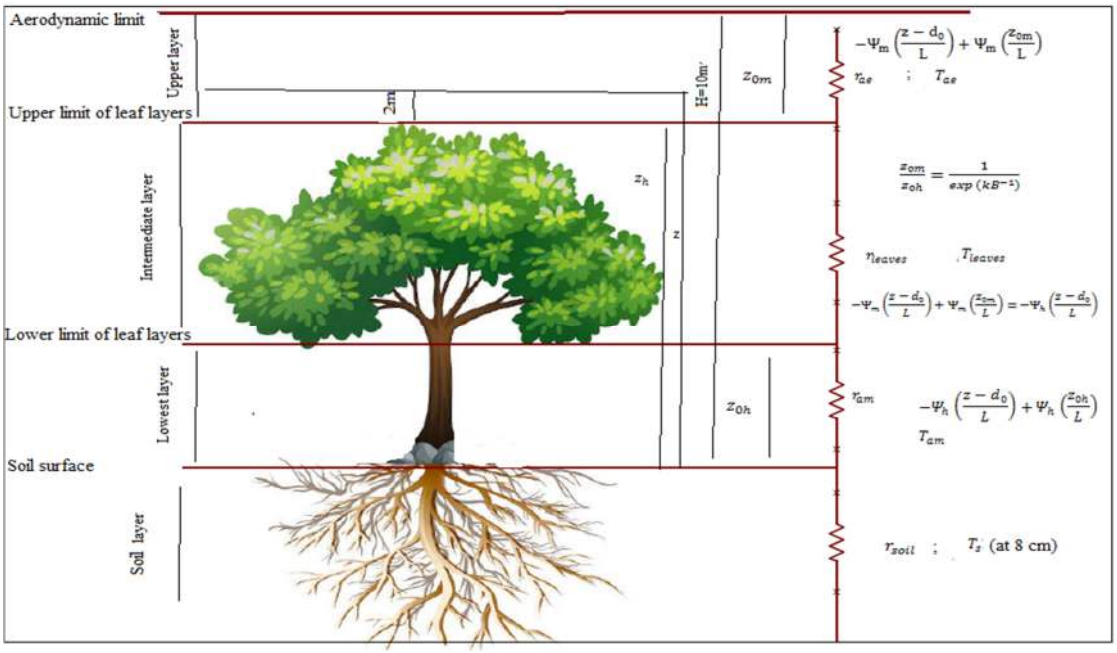


***Fig. 1. Conditions for finding equilibrium between the stability correction functions for quantities of motion and sensible heat transfer***

In the intermediate layer, thermomechanical equilibrium is reached when $K = 1$, which corresponds to an equilibrium between the thermal and mechanical properties, i.e. $k' = 1$ et $-\Psi_m\left(\frac{z-d_0}{L}\right)+\Psi_m\left(\frac{z_{0m}}{L}\right) = -\Psi_h\left(\frac{z-d_0}{L}\right)+\Psi_h\left(\frac{z_{0h}}{L}\right)$.

According to the first principle of thermodynamics, all systems naturally seek a state of equilibrium. Unfortunately, because of the variability of meteorological parameters, thermomechanical equilibrium is never reached outside the intermediate layer. In the search for a state of thermomechanical equilibrium, an expression for the sensible heat flux has been derived from the momentum stability correction function (inflow) and the sensible heat transfer correction function (outflow of leaf density) :

$$\frac{z_{0m}}{z_{0h}} = \frac{1}{exp(kB^{-1})} * k'.\frac{-\Psi_m\left(\frac{z-d_0}{L}\right)+\Psi_m\left(\frac{z_{0m}}{L}\right)}{-\Psi_h\left(\frac{z-d_0}{L}\right)+\Psi_h\left(\frac{z_{0h}}{L}\right)} \text{ [Eq. 22]}$$

where $k' = \frac{k_2}{k_1}$, with $k_1 = \frac{r_{leaves}}{r_a}$ and $k_2 = \frac{r_{soil}}{r_{leaves}}$.

The heat flux from the sun passes through the layers of plant leaves and cloud cover to penetrate the soil, according to the proportional relationship below:

$$k' = \frac{(r_{leaves})^2}{r_a * r_{soil}} \text{ [Eq. 23]}$$

Where $r_{leaves} = \frac{\sum_{n_i=1}^{n_f} r_{leave(i)}}{n_f - n_i}$

Equation [Eq. 21] becomes :

$$-\Psi_h\left(\frac{z-d_0}{L}\right) + \Psi_h\left(\frac{z_{0h}}{L}\right) = k' * \left(-\Psi_m\left(\frac{z-d_0}{L}\right) + \Psi_m\left(\frac{z_{0m}}{L}\right)\right) \text{ [Eq. 24]}$$

Relations [Eq. 18] and [Eq. 24] allow us to write:

$$-\Psi_h\left(\frac{z-d_0}{L}\right) + \Psi_h\left(\frac{z_{0h}}{L}\right) = k' * \left(\left(\frac{\mu}{\mu_*}\right).k - ln\left(\frac{z-d_0}{z_{0m}}\right)\right) \text{ [Eq. 25]}$$

From the equations established above, the expression for sensible heat was finally established. The net energy balance model is based on realistic physical conditions, which makes it more favourable and usable in environmental conditions where climatic variations are felt [53, 54]. The relationship between the sensible heat flux of a soil surface covered with vegetation is given by :

$$H = k.\mu.\frac{\rho_{air}.C_{P,air}}{r_{soil}+r_a+r_{leaves}}.(T_s - T_a).\left[ln\left(\frac{z-d_0}{z_{0h}}\right) + K * \left(\left(\frac{\mu}{\mu_*}\right).k - ln\left(\frac{z-d_0}{z_{0h} * exp(kB^{-1})}\right)\right)\right]^{-1} \text{ [Eq. 26]}$$

The relative $(\Lambda_r)$ and real $(\Lambda)$ evaporative fractions were evaluated by [55] :

$$\Lambda_r = \frac{\lambda.E}{\lambda.E_{wet}} = 1 - \frac{H - H_{wet}}{H_{dry} - H_{wet}} \text{ [Eq. 27]}$$

And,

$$\Lambda = \frac{\lambda.E}{R_n - G_0} = \frac{\Lambda_r.\lambda.E_{wet}}{R_n - G_0} \text{ [Eq. 28]}$$

$E_{wet}$ : evaporation from the ground surface; $\gamma$ : psychrometric constant; $H_{wet}$ : sensible heat flux in wet conditions; $H_{dry}$ : sensible heat flux in dry conditions.

Recent models for estimating evapotranspiration from plant cover dissociate evaporation from the soil surface from transpiration from the plant cover and their interception. Evapotranspiration simulates changes in canopy structure and stomatal resistance. The Penman-Monteith formula was used, the advantage of which was that it took into account the evapotranspiration of a closed plantation [55, 56]. The balance of the energy balance at the surface of the plant cover results from the balance of the energy fluxes of all the surfaces present: leaves, stems and soil surfaces. This involved defining the expression of the sensible heat flux of the soil-plant-atmosphere system [47] by superimposing the layers that exchange energy. For gaseous exchange, leaf surfaces were considered to have the same temperature and the same average stomatal resistance. Since the leaf resistances were considered to be connected in series, the sensible heat fluxes under dry and wet conditions were calculated:

$$\begin{cases} H_{wet} = \dfrac{(R_n - G_0)_{wet} - \dfrac{\rho_{air}.C_{P,air}}{r_a + r_{leaves} + r_{soil}} . \dfrac{e_S.e_a}{\gamma}}{\left(1 + \frac{\Delta}{\gamma}\right)} \ (a) \\ \lambda.E_{wet} = (R_n - G_0)_{wet} - H_{wet} \ (b) \\ H_{dry} = (R_n - G_0)_{dry} \ (c) \end{cases} \text{ [Eq. 29]}$$

The resistance to turbulent transfer was estimated by considering theoretical approaches, in particular those of Businger *et al.,* (1971) [62]. These approaches are based on the use of logarithmic profiles of mass and energy transfer in the ground surface boundary layer and the ground surface-atmospheric air surface boundary layer coupling operated at the flux level on the basis of the convective boundary layer. Integration of the wind speed and friction profiles leads to two similarity functions ($\psi_m$ and $\psi_h$). These functions are parameterised by the regime of convective exchanges of quantities of movement and heat. In SEBAL models, the resistance to turbulent transfer expresses the introduction of plant parameters [23]. Thus, the resistance to water vapour diffusion in the soil is defined by the relationship [63] :

$$r_{soil} = exp\left(a_{rss} - b_{rss}\frac{\theta^*}{\theta^*_{Sat}}\right) \text{ [Eq. 30]}$$

$a_{rss} = 8.2$ and $b_{rss} = 4.3$ are empirical constants whose values are given by the authors; $\theta^*$ : soil water content measured between 0 and 5 cm in the soil (%) ; $\theta^*_{Sat}$ **:** water content at soil saturation (%).

The equivalent air resistance is given by:

$$r_a = r_{ae} + r_{am} \text{ [Eq. 31]}$$

The characteristic parameters of the aerodynamic boundary layer used to calculate the aerodynamic resistance were measured at a height of 10 metres. This resistance is expressed as follows [20] :

$$r_{ae} = \frac{1}{k^2.\mu_{2m}}.ln\left(\frac{Z-d_0}{Z_{0m}}\right).ln\left(\frac{Z-d_0}{Z_{0h}}\right) \text{ [Eq. 32]}$$

And the air resistance of the layer below the canopy is deduced from that of the leaf layer, and the aerodynamic resistance is calculated as follows:

$$r_{am} = \frac{r_{leaves} - \frac{r_{ae}}{r_{leaves}}}{r_{leaves}} \text{ [Eq. 33]}$$

Vidal (1989) [47] used the expression of Perrier (1982) to calculate the length of thermal roughness as a function of leaf area index and canopy height

$$z_{0h} = \left(1 - \exp\left(-\frac{LAI}{2}\right).\exp\left(\frac{\left(-\frac{LAI}{2}\right)}{Z_h}\right)\right) \text{ [Eq. 34]}$$

The values of the parameter $k.B^{-1}$ for a surface covered with vegetation were calculated using the relation [18] :

$$k.B^{-1} = \frac{k.C_d}{4.C_t.\left(\frac{\mu_*}{\mu}\right)\left(1-\exp\left(-\frac{n^*}{2}\right)\right)}f_C^2(\xi) + 2.f_C(\xi).f_S(\xi).\frac{k.\left(\frac{\mu_*}{\mu}\right)\left(\frac{Z_{0m}}{Z_h}\right)}{C_t^*} + KB_S^{-1}.f_S^2(\xi) \text{ [Eq. 35]}$$

$C_t = 0.01$ : Canopy heat transfer coefficient; $\mu_*$ : friction velocity or friction speed in m/s; $\mu$: wind speed measured at 2 metres and 10 metres; $C_d = 0.2$ : leaf flow resistance coefficient; $C_t^*$ : soil heat transfer coefficient; $n^*$ : model parameter.

The $n^*$ parameter is a function of the ratio of friction speed to wind speed, the leaf area index, the coefficient of resistance to leaf flow and the heat transfer coefficient of the plant canopy. This parameter is calculated using the relationship [59**,** 51] :

$$n^* = \frac{C_d.LAI}{2.\left(\frac{\mu_*}{\mu}\right)^2} \text{ [Eq. 36]}$$

The ratio between friction speed and wind speed is given by the expression:

$$\frac{\mu_*}{\mu} = 0{,}32 - 0.2.exp(-15{,}1).LAI \text{ [Eq. 37]}$$

The ground heat transfer coefficient $(C_t^*)$ is given by the equation:

$$C_t^* = {P_r}^{-2/3}.{R_e}^{-1/2}$$ [Eq. 38]

$P_r$: Prandtl number with a value of 0.7; $R_e$ : Reynolds number.

The Reynolds number is calculated as follows:

$$R_e = \frac{h_S.\mu_*}{\nu}$$ [Eq. 39]

$h_S$ : height of ground roughness, assumed constant with a value of 0.009 m; $\nu$ : kinetic viscosity of the air.

The friction speed is a fictitious function that considers the variation in the intensities of the transfers of momentum and heat as being constant and homogeneous phenomena. The kinetic viscosity of air is calculated by the formula :

$$\nu = 1{,}327.10^{-5}\left(\frac{P_0}{P}\right)\left(\frac{T_S}{273{,}16}\right)^{1{,}81}$$ [Eq. 40]

$P_0$ : standard atmospheric pressure with a value of 1013.15 hPa; $P$ : atmospheric pressure measured at the site.

The estimated parameter ${kB^{-1}}_S$ on a bare ground surface is given by the relation [23] :

$$kB_S^{-1} = 2{;}46.{R_e}^{1/4} - ln(7{,}4)$$ [Eq. 41]

The height of the zero displacement plane is defined by the expression :

$$d_0 = \frac{3}{4}z_h$$ [Eq. 42]

The density of air is expressed by the relationship [26] ***:***

$$\rho_{air} = \frac{P}{R_a.T_a}\left(1 - \frac{0{,}378.RH_a.e_S}{P}\right)$$ [Eq. 43]

$R_a = 287{,}04\,\frac{J}{Kg.°K}$ : gas constant for air; $RH_a$ : relative air humidity (%).

The relative humidity of the air is related to the specific humidity of the air $q_a$ $(Kg_{water}/Kg_{hmid\ air})$ by the relationship:

$$q_a = 0.622.\left(\frac{P}{RH_a.e_S} - 0{,}378\right)$$ [Eq. 44]

The psychrometric constant $(\gamma)$ is defined by [27] :

$$\gamma = \frac{C_P}{\lambda} = \frac{C_P.P}{0.622.\lambda}$$ [Eq. 45]

$C_P$: specific heat of air at constant pressure (J/kg/°K) ; $\lambda$ : latent heat of vaporisation (J.kg$^{-1}$).

The correction for the specific heat intensity of the air at constant pressure takes into account the specific humidity of the air and the latent heat of dry air according to the relationship [28] :

$$C_P = (1 + 0{,}84.q_a).C_{Pd}$$ [Eq. 46]

$C_{Pd}$: latent heat of dry air ($\approx 1004{,}64$ J/Kg/°K).

The specific latent heat of vaporisation $(\lambda)$ is expressed by :

$$\lambda = 4{,}2.\big(597 - 0{,}6.(T_a - 273)\big).1000$$ [Eq. 47]

The Clausius-Clapeyron equation is used to calculate the saturation vapour pressure gradient at room temperature. This function relates the saturation vapour pressure of the air to the ambient temperature:

$$\Delta = \frac{373.15 e_S}{{T_a}^2}\left(13.3185 - 3{,}952T_{rad} - 1{,}9335{T_{rad}}^2 - 0{,}5196{T_{rad}}^3\right)$$ [Eq. 48]

with $T_{rad}$ : radiometric temperature

The radiometric temperature is calculated by the equation:

$$T_{rad} = \left(f_C(\xi).T_{veg}^4 + f_S(\xi).T_S^4\right)^{\frac{1}{4}}$$ [Eq. 49]

$T_{veg}$ : Canopy temperature, measured by an IR-8BT infrared thermal camera with a 80x80 pixel infrared image for temperature ranges from -20° to +380°C.

The air vapour pressure at saturation $(e_S)$ is calculated using the relationship [65] :

$$e_S = P_0.exp\left(13{,}3185.T_{rad} - 1{,}976{T_{rad}}^2 - 0{,}6445{T_{rad}}^3 - 0{,}1299{T_{rad}}^4\right)$$ [Eq. 50]

#### 2.2.2.1.4 Assessment Of Latent Heat Or Potential Evapotranspiration

Latent heat is the energy equivalent of evapotranspiration and refers to the processes involved in transforming water from a liquid to a gaseous state. This heat represents the height of water evaporated per unit of time. This energy promotes a change in the state of water at the soil surface and plant transpiration through the leaves, resulting in a vapour pressure gradient and a renewal of the air mass (turbulence). The contribution of transpiration to evapotranspiration is variable and can reach almost 100% for dense plant cover. Evapotranspiration is an appropriate index of the moisture status of the soil surface on a timescale [32] known as real evapotranspiration. It is the sum of the heat flux evaporated by the soil surface and the heat flux transpired by the vegetation, corresponding to the residual of the energy balance. The expression for evapotranspiration $(\lambda.E)$ can be deduced from equation [Eq. 26 (b) ] [66] :

$$\lambda.E = \Lambda.(R_n - G_0)$$ [Eq. 51]

#### 2.2.2.2 Estimating The Conductive Energy Flux Of Cultivated Land

The conductive heat of cultivated land, calculated under in situ conditions, is governed by variations in environmental thermohydric properties (radiation balance, amount of rainfall, relative air humidity) and biophysical properties (plant properties, wind speeds). By modelling the above parameters, the soil conductive heat flux equation is deduced from the net closed energy balance equation:

$$G_0 = R_{net} - (H + \lambda E)$$ [Eq. 52]

### 2.2.3 Interaction Between Turbulent Energy Fluxes ($Rn-G0$) And Available Energy Fluxes ($H+\lambda E$)

Turbulent energy expresses the energy losses produced on a given surface, whereas available energy is the energy supplied to this surface to meet the needs of users. The interactions between turbulent and available energy fluxes can be understood [61, 62] by calculating the difference between the heat flux from net solar radiation and the conductive heat flux from the ground as a function of the sum of sensible and latent heat fluxes.

## 3 Results And Discussion

### 3.1 Average Hygrothermal Potential Over Eleven Years (2011-2021)

#### 3.1.1 Monthly Variations In Mean Global Solar Irradiation, Rainfall And Relative Humidity (2011-2021)

Figures 2a and 2b show the monthly variations in relative humidity, global irradiation and average rainfall measured over 11 years. In Figure 2a), the relative humidity of the air increases from 65% to 82% with rainfall (from 0.7 mm/day to 7.5 mm/day), with the highest values observed in June and October, with 7.5 mm/day and 6.9 mm/day respectively and an average monthly humidity of 80%. As for Figure 2b), average monthly global irradiation is high from mid-November to April and from mid-July to mid-September, with an average of 496 Wh /m²/month, for low rainfall. Contradictory trends are observed in the period from mid-May to mid-October, with an average of 450 Wh /m²/month.

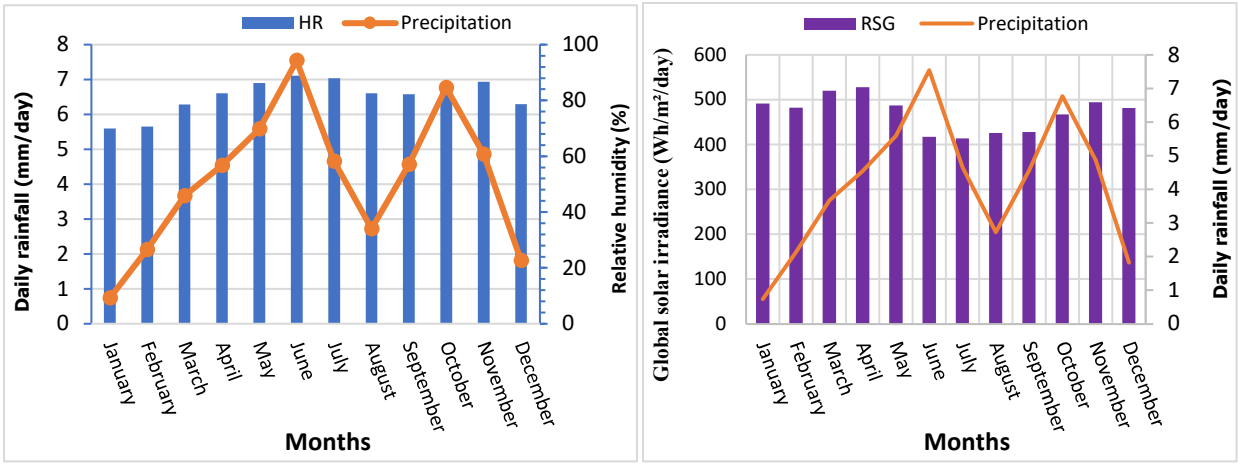


a) b)

***Fig. 2. Average monthly variations in ambient air humidity, global solar irradiance and daily precipitation***

Figures 3a) and 3b) show the monthly and annual variations in average rainfall over the 11 years. Analysis of Figure 3a) shows that June and October have more rainfall, with 35 mm/month and 35.1 mm/month respectively, whereas January and February have less rainfall, with 1.1 mm/month and 2.4 mm/month respectively. In addition, the months of May, June, September and October have average rainfall of over 20 mm/month. An analysis of Figure 3b) reveals rainfall variability over the eleven years. The years 2013, 2015, 2017 and 2021 have average rainfall in excess of 50 mm/month. From 2013 to 2020, there is a downward trend in annual rainfall.

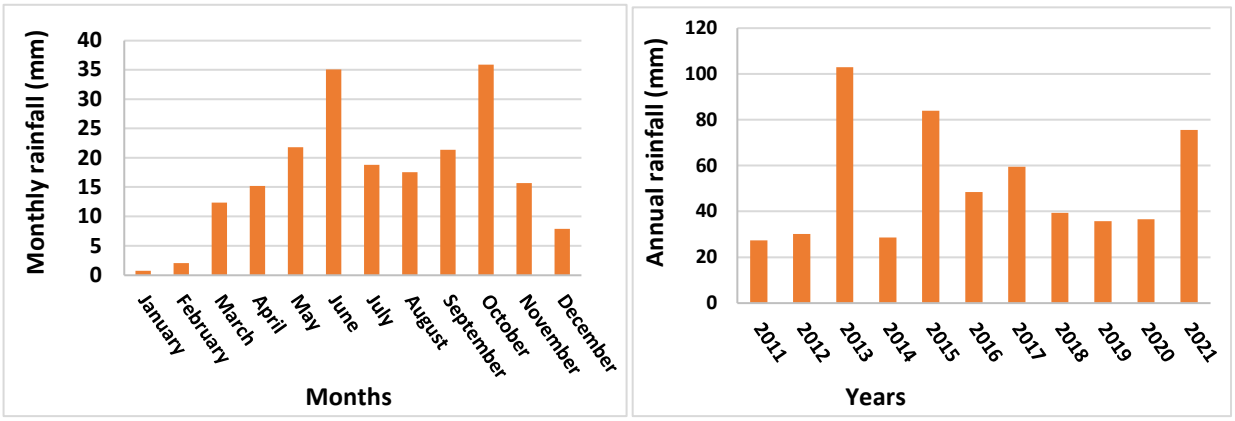


(a) (b)

***Fig. 3. Precipitation variations: (a) monthly and (b) annual***

From the above analyses, it can be deduced that the Yamoussoukro area has two rainy seasons: the main rainy season, which extends from mid-May to mid-July, and the short rainy season, which runs from mid-September to mid-November. The two main rainy seasons are identified by rainfall peaks. The rainy seasons mark the growth of plants that produce pollen grains and other fine plant particles that can be transported by natural (mainly wind and run-off water) and man-made agents. The combination of plant particles and dust particles in the air forms aerosols [69]. During rainy seasons, pronounced vertical wind shear profiles are created, leading to a high degree of convective organisation. In addition, the sky is cleaned by the large quantities of rain that eliminate aerosol loads. Produced from the cloud layers, the relative humidities and large amounts of rain increase the intensity of diffuse irradiation, providing a small amount of solar radiation reaching the earth's surface. According to the work of Kniffka *et al.* (2019) [36], precipitation destabilises local radiation budgets. Pante *et al.* (2021) [70] analysed spatio-temporal variations in precipitation, aerosols, radiation, clouds and visibility at surface stations and in space to identify potential indicators of anthropogenic air pollution on rainfall trends. To do this, they used meteorological data from 1983 to 2017. The results of their work showed that rainfall in dry seasons in the Yamoussoukro area remains below 4 mm/day,

while it is around 8 mm/day in rainy seasons, with relative humidity of up to 95%. These results confirm those obtained in our studies. The results of their work went on to show that climate trends in the Yamoussoukro region have been decreasing rainfall since 2015, which is in line with our results. The Yamoussoukro region, on the other hand, has two dry seasons: the short dry season between mid-July and mid-September, and the long dry season between mid-November and April. The four seasons alternate in such a way that the rainy seasons are interrupted by the dry seasons. In the dry seasons, aerosol movements are increased by the cessation of heavy rain and the drying of the air [71]. From November onwards, we see the arrival of the harmattan, which produces significant advection from the southern monsoon and transports aerosols over long distances. These phenomena increase cloud cover, reducing horizontal visibility and radiation at the earth's surface. The moderation of the strong winds caused by the rapid retreat of the monsoon in February favours an increase in the amount of irradiation. Maranan et al. (2018) [71] studied the relationship between weather, climate and air pollution in southern West Africa from 1998 to 2013. The results of their work gave profiles similar to those observed in our work.

### 3.1.2 Monthly And Annual Variations In The Clarity Index From 2011 To 2021

Figures 4a), b, c, and d) illustrate the monthly and annual profiles of the lightness index in the Yamoussoukro region. Analysis of this figure allows us to classify the monthly evolution of the clarity index into two categories:

- Class 1: from November to February, the lightness index falls from 0.577 to 0.47, and from July to September, it falls from 0.64 to 0.54.
- Class 2: from March to June, the clarity index increases from 0.61 to 0.64, and from mid-September to October, the clarity index increases from 0.54 to 0.58.

In addition, the monthly trend shows that the clarity index varies between 0.26 and 0.7. Finally, annual variations in the clarity index (Figures 4b, c, and d) show an irregular, non-linear character with rainfall from one year to the next. This makes it difficult to compare rainy years based on annual values. However, the values of this index give an indication of its variational range for a given region.

Yéboua *et al.*, (2019) [72] carried out a study based on one year's data (2017) to classify solar radiation in the Yamoussoukro region. The method of averages of the brightness index was used with a distribution independent of season and site. The results showed a variation in lightness index from 0 to 0.7 for processed data. This first range is in line with the results of our studies. However, the second range of clarity index values in their studies varied from -1 to 0.7 for biased data. Since the clearness index is a parameter varying from 0 to 1 [73], this range shows not only the incapacity of their method, but also that their study, which used data from a single year, will not be able to be generalized because of the high climatic variability. Ayodele and Ogunjuyigbe (2015) [73]

studied monthly, seasonal and annual variations in global solar radiation, brightness index and scattering fractions at Alice (South Africa) using eight years of data (2000–2008). The results of their work showed that the largest mean value of the clearness index was 0.62 and the smallest mean value was 0.54, obtained in summer and winter, respectively, compared with large and small values of 0.66 and 0.58 obtained in our study, respectively.

The clearness index is an atmospheric attenuation characteristic that fluctuates with season, geographical location, time of year and climatic conditions. The small clarity index values of 0.33, 0.29 and 0.35 were obtained in July, August and September, respectively, confirming the results of our studies. The higher the rainfall, the higher the clarity index. Apeh et al. (2021) [37] evaluated monthly, seasonal and annual variations in global solar radiation, the clarity index and diffuse fractions in Alice, South Africa, from 2017 to 2020. The results of their work showed that the clearness index evolves with monthly rainfall but, inversely, with global irradiance. The maximum values of the clarity index (0.74) were obtained in rainy seasons, when the earth's surface faces the sun, compared with the low values of 0.11 obtained in dry seasons, when the earth's surface is inclined to that of the sun. Furthermore, they concluded that the clarity index is influenced not only by atmospheric conditions such as dust and turbidity, but also by the sun's movements. The large discrepancies observed between mean and minimum values in the rainy season reflect unstable weather conditions due to high humidity, the presence of shifting cloud layers, and fluctuating solar radiation at the earth's surface. In the dry season, however, the sky is in a state of dynamic stability.

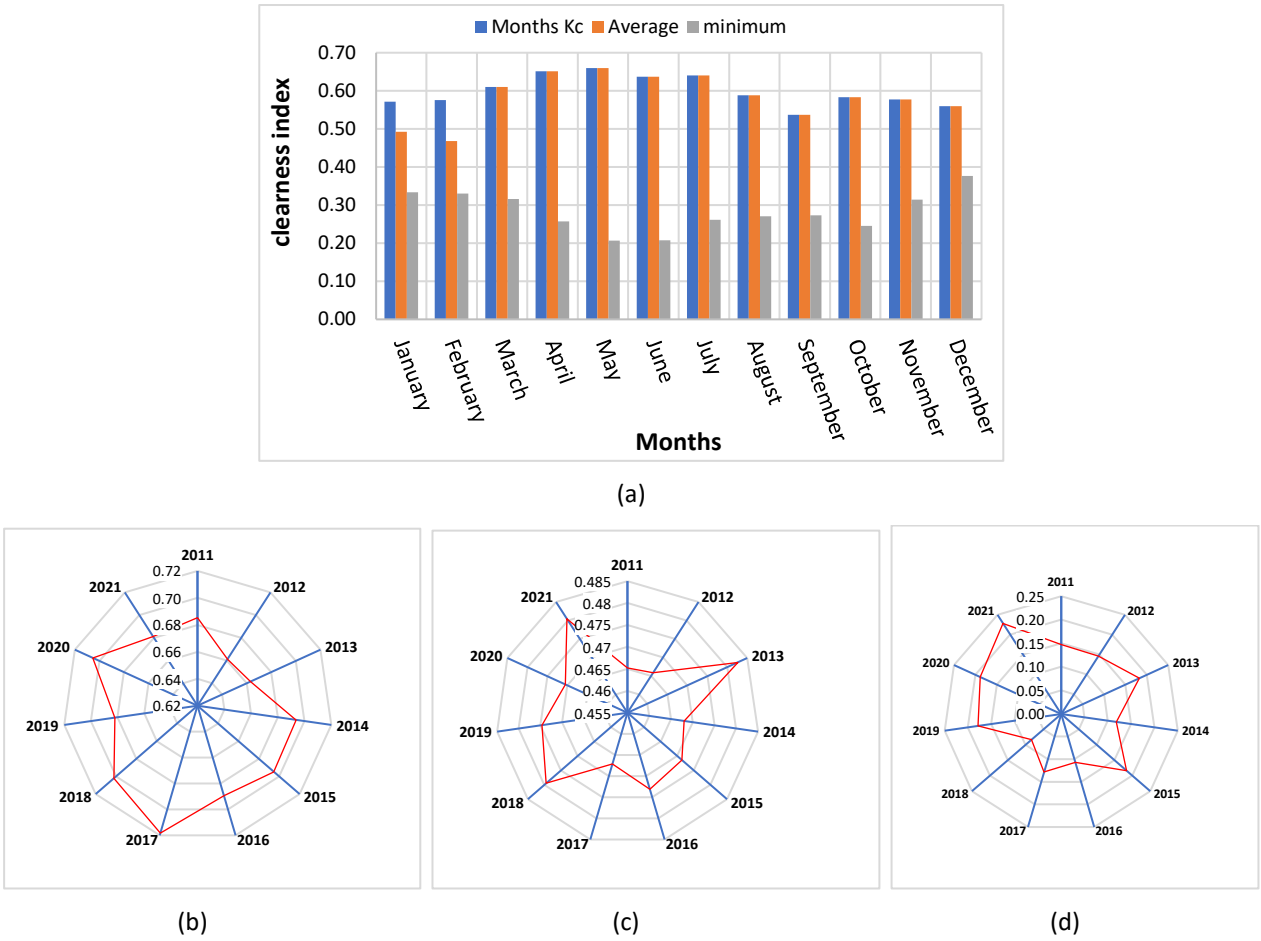


*Fig. 4. Variations in the clearness index in the Yamoussoukro region: (a) : monthly, (b) : annual maximum, (c) : annual averages and (d) : annual minimum.*

### 3.2 Energy Balance In Cultivated Land Based On Biophysical Parameters

#### 3.2.1 Biophysical Parameters Of Cocoa Crops And Evaporative Fractions

##### 3.2.1.1 Leaf Area Index

Figure 5 illustrates the variation profile of the monthly leaf area index. Analysis of this figure shows that LAI increases progressively from May, with a value of 3.5 m²/m², to October, with a maximum of 5.4 m²/m². Outside this range, LAI drops and remains virtually constant with values below 3 m²/m². Overall, LAI rose from 2 m²/m² to 5.42 m²/m².

Leaf area index (LAI) provides information on crop growth trends over the year. It represents one of the most important biophysical parameters of plants. LAI is a decisive parameter for understanding the state of crop development. Leaf area increases with rainfall, which shows an increase between April and October, with a discontinuity marked by the late effects of the short dry season between September and October. In the dry seasons, the drying out of the leaves reduces the density and thickness of the leaves produced by the increase in radiative balances. Our results were confirmed by those of [47, 52, 69].

In fact, from December to mid-April, crops are in a state of thermal stress governed by a water deficit (drop in relative air humidity and rainfall), reducing leaf size and sometimes contributing to the loss of some leaves. With the presence and gradual increase in rainfall and relative air humidity observed from April onward, leaf surfaces increase along with plant organs until they reach their maximum size. Leaf size remains almost constant until a new thermal cycle produces opposite effects. Zhao et al. (2020) [50] proposed a probability theory-based method for estimating canopy fraction using leaf area index and global leaf agglutination index monthly from 2013 to 2015 in Europe. The results of their study showed that LAI varies between 3 m²/m² and 8 m²/m². This range is higher than that obtained in our study because the food crops they studied grew strongly

with the canopy in rainy seasons. Unlike the rice plants, the cocoa trees we studied had already reached maturity and did not undergo any particular variation in size, apart from their leaves. Goswami *et al*., (2015) [75] studied the relationships between LAI, biomass and leaf area index for six plant species in Barrow, Alaska, from 1972 to 2008. Results showed LAI variation from 0.83 m²/m² to 6 m²/m². They noted that LAI increased with biomass and was a function of plant species.

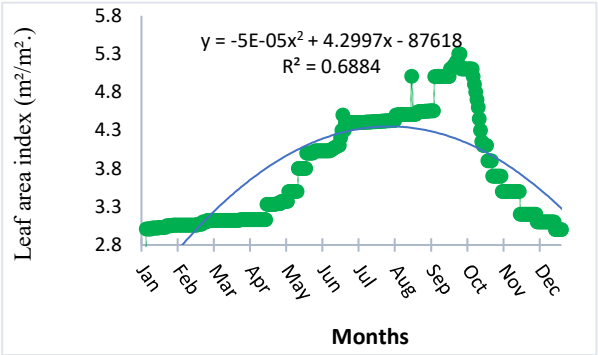


***Fig. 5. Variation in leaf area index (LAI)***

#### 3.2.1.2 DAILY AND ANNUAL VARIATIONS IN RELATIVE AND REAL EVAPORATIVE FRACTIONS

Figures 6a) and 6b) respectively illustrate the results of daily and annual variations in the fraction of water likely to be evaporated, known as the relative evaporative fraction or potential evapotranspiration (ETP), and the fraction of water evaporated, known as the real evaporative fraction or real evapotranspiration (ETR). According to figure 6a), the relative evaporative fraction shows a high frequency of dispersion from November to April, with values ranging from 0.35 to 0.9 mm/day, with an average of 0.51 mm/day. Relative evapotranspiration is high and continuous from May to July and in October, with intensities ranging from 0.6 mm to 0.7 mm per day. As for the analysis of the profile of the actual evaporative fraction, values are practically constant in the dry seasons at 1.5 mm/day, and increase in the period from May to October, varying from 2 mm/day to 6 mm/day.

Analysis of Figure 8b) shows that the years 2011–2016 and 2020 have average relative evaporative fractions greater than 1 mm/year. In particular, the years 2015 and 2016 have high average relative evaporative fraction values between 1.4 and 1.7 mm/year. If we consider the evolution of real annual evaporative fractions, we see that they vary from 5 mm/year to 120 mm/year. The years 2015 and 2021 show the highest values of real evapotranspiration, with 82 mm/year and 119 mm/year, respectively.

Liu et al. (2019) [76] examined the variation of the actual evaporative fraction from the relative evaporative fraction at hourly, diurnal and daily scales calculated and measured by Eddy's Covariance technique at different stages of the 2015 and 2016 rice evolution in China. The results showed that the relative evaporative fraction varies during rice growth from 0.8 to 0.92 mm/day with an average of 0.79 mm/day and reaches a maximum of 1 mm/day during the late maturity phase of the plant. Daily values of this fraction are high at sunrise and sunset, due to high ambient humidity, and decrease with increasing solar radiation intensity. Moreover, this fraction decreases sharply with decreasing soil moisture. The difference in seasonal evaporative fraction values is attributed to the phenological characteristics of crops, which are influenced by weather conditions.

In addition, the results of their work showed actual evaporative fractions ranging from 0 to 3.835 mm/day and from 0 to 3.816 mm/day in 2015 and 2016, respectively. The relative evaporative fraction values obtained in their study are lower than those in our study, although they worked on annual crops. On the other hand, annual crops grow rapidly throughout the year, but have lower evaporative fraction values than multiannual crops. As for cocoa crops, despite the slow evolution of their evaporative fraction, they have maximum values because they have reached maturity (crops over 15 years old). The results of Liu et al. agree with those of our work. Timmermans *et al*, (2013) [77] evaluated the actual evapotranspiration of a rice field, and the results of their study gave an average daily variation of between 0 and 7 mm/day, while relative evapotranspiration ranged from 0 to 14 mm/day. From July to August, the actual evaporative fraction varied from 3.14 mm to 6.73 mm per month. The values of this fraction are higher than those of our work, as these authors worked in a subtropical climate in the presence of cold monsoon winds, which increased relative humidity and reduced the intensity of global solar radiation. They also concluded that actual evapotranspiration increases with leaf area index. According to the findings of Chávez et al. (2008) [78], weather instability is felt on a small (hourly) scale. It is therefore recommended to carry out a large-scale assessment (daily,

monthly or annual) of actual evapotranspiration to overestimate its values. This actual evapotranspiration is largely influenced by available surface energy. Wu *et al.* (2015) [67] evaluated annual actual evapotranspiration in 2011 and China. The results gave an annual average value of 270.6 mm per year. This value is significantly higher than that of our study due to the low solar potential in their study area.

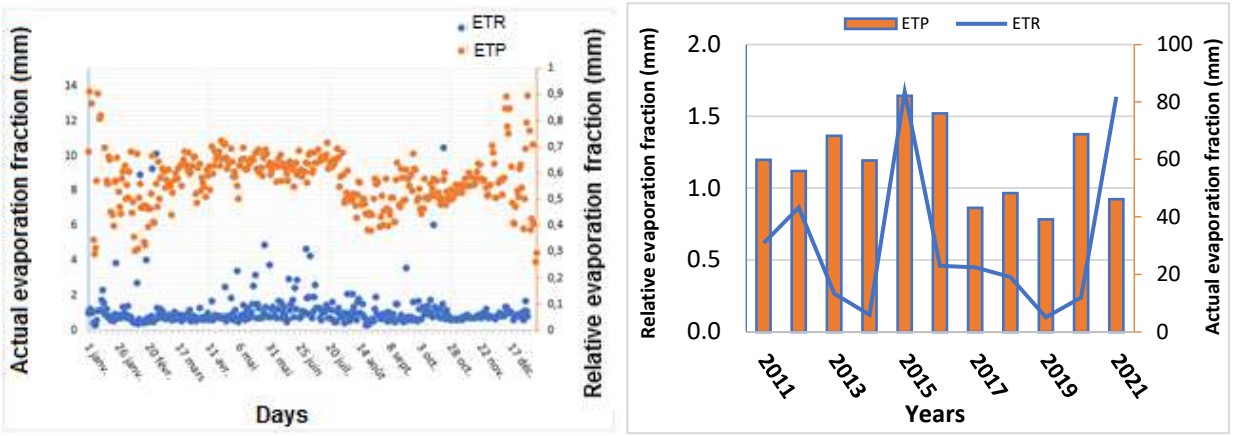


(a) (b)

***Fig. 6. Daily and annual variations in relative and real evaporative fractions***

### 3.2.2 ENERGY BALANCE IN CULTIVATED LAND

Table I shows the average values of energy fluxes modelled for cocoa-growing land over eleven years (2011–2021). Analysis of this table gave mean values for net solar radiation heat flux of 221.405 Wh/m$^2$/year, latent heat flux of 44.290 W/m$^2$/year, sensible heat flux of 218.592 W/m$^2$/year, and conductive heat flux of -22.270 W/m$^2$/year.

Moorhead *et al.*, (2017) [74] evaluated the average energy flux values using a lysimeter and scintillometer. The results of the study showed that sensible heat measured with a lysimeter varied from -761.7 to 426.4 W/m$^2$, with an average of -11.4 W/m$^2$. The lysimeter gave a wider range of sensible heat values than the scintillometer, due to the measurement scales associated with the two different types of equipment.

***Table 1. Average energy flux***

| Average $R_n$ (W/m²/year) | Average $H$ (W/m²/year) | Average $\lambda E$ (W/m²/year) | $Average\ G_0$ (W/m²/year) |
|---|---|---|---|
| 221,405 | 44,290 | 218,592 | -22,270 |

Figures 9a) and 9b) show, respectively, the daily and monthly variations in the soil energy balance. Analysis of Figure 9a) shows that latent and sensible heat fluxes evolve in contradictory ways. Net solar radiation heat flux and latent heat flux have the highest values, while conductive energy flux and sensible heat flux have the lowest. The sequential analysis of energy flux trends was carried out by splitting their annual profile into three parts: from January to April (period 1), from May to September (period 2), and from October to the end of December (period 3). High values for net solar radiation heat flux and sensible heat flux are obtained in periods 1 and 3. In period 1, net solar radiation heat flux, sensible heat flux and conductive heat flux (in absolute values) are high. Net solar radiation heat flux and sensible heat flux decrease from 250 W/ m$^2$/day to 230 W/ m$^2$/day and from 150 W/ m$^2$/day to 50 W/m$^2$/day, respectively, while conductive heat increases from -50 W/ m$^2$/day to -10 W/ m$^2$/day. In period 3, net solar radiation heat flux and sensible heat flux undergo progressive increases to reach new high values, as does conductive heat, which decreases, but with lower intensities than in period 1. However, in period 1, latent heat flux has lower intensities than net radiation heat, while the opposite phenomenon occurs in period 3.

During period 2, the conductive heat flux undergoes a strong dispersion, governed by the daily variability of the latent heat flux. Conductive heat increases from -10 W/m²/day to 45 W/m²/day until the end of September. During this period, the latent heat flux increases from 150 W/m²/day to almost 300 W/m²/day, reaching higher values than the net solar radiation energy flux, and then decreases from July onwards, reaching low values in August. In contrast to latent heat flux, net solar radiation

heat flux and sensible heat flux decreased to low intensities of 245 W/ $m^2$/day to less than 200 W/$m^2$/day and 50 W/$m^2$/day to 10 W/$m^2$/day, respectively, in August.

Analysis of the monthly energy fluxes in ascending order (Figure 9b), showed that February (in period 1) and November (in period 3) have the lowest amounts of conductive heat in the year, with -55 W/$m^2$/month and -40.5 W/$m^2$/month, respectively. In contrast, in period 2, the month of July shows the highest levels of conductive heat, with 14 W/$m^2$/month. In absolute terms, conductive heat evolves in the same direction as sensible heat flux and net solar radiation flux.

Energy and water exchanges between the components of the soil-plant-atmosphere system at the earth's surface are produced by the radiation balance, plant transpiration and evaporation from water and soil surfaces. These processes have a considerable impact on the energy balance within the soil. While latent heat explains the transpiration of plant leaves and the evaporation of water surfaces in the universe [77, 78], sensible heat explains the evaporation of soil surfaces in the atmosphere. The combination of latent and sensible heat results in evapotranspiration. Latent heat fluxes are energy losses produced by aerodynamic and hydric factors (soil water and canopy water) that destabilize the large quantities of solar energy in the soil.

The above-mentioned system operates as an open system, exchanging heat, water and matter [29] between its three components in the search for thermo-hydric equilibrium between them. Solar radiation is the only source of energy for this process, whose intensities at the earth's surface are represented by the heat flux of net solar radiation. Part of the solar radiation is reflected by airborne particles, plant cover and soil mineral surfaces, and the remaining part of the radiation flux is absorbed by the soil, increasing its conductive heat (in absolute terms) and sensible heat. Conductive heat flux is higher the drier the ground surface and the clearer the sky. These facts lead to a decrease in latent heat flux in the dry season and are contrasted in the rainy season. From October to the end of December, despite the high intensity of net solar radiation, the quantities of sensitive and conductive energy fluxes are lower than in the period from January to April, due to the presence of the harmattan, which are dynamic factors contributing to the reduction of net solar radiation intensities through the contribution of the cool monsoon winds. The overall observation of monthly and annual variations in heat fluxes enables us to group them into two classes: class 1 is made up of periods 1 and 3 with negative conductive heat flux values, and class 2 is made up of period 2 with largely positive conductive heat fluxes.

The negative signs explain thermal penetration into the soil (energy gain for the soil), while the soil loses its energy [81] (represented by the positive sign) with the universe by plant transpiration, explained by the increase in turbulent energy (presence of rain and ambient humidity, wind). When plant leaf density decreases, it contributes to an increase in conductive heat flux. This was observed in the work of Taylor et al. (2019) (2019) [69] and Pante *et al.* (2021) [70], who found that deforestation and urbanization enhance convective triggering by increasing turbulent fluxes of sensible heat. Latent energy is the main consuming source of radiant energy fluxes [76], which decrease sensible and conductive energy fluxes. The reasons are governed by the decrease in plant transpiration rates during the plant growth phase and the increase in advection observed when latent heat flux exceeds net solar radiation heat flux which decrease sensible and conductive energy fluxes. The reasons are governed by the decrease in plant transpiration rates during the plant growth phase and the increase in advection observed when latent heat flux exceeds net solar radiation heat flux [74].

Nelli *et al.*, (2019) [42] evaluated the closure of the surface energy balance in an arid environment through a comprehensive analysis of surface radiation and heat fluxes at seasonal and diurnal time scales using the Eddy Covariance method. The results showed that sensible heat flux intensity remains below 20 W/$m^2$ throughout the year, while latent heat flux intensity is below 30 W/$m^2$. The differences in amplitudes are due to differences in climatic conditions. Their study area has an arid climate, so the high east wind speed allowed cooling of the plant canopy surfaces. This contributes to a reduction in surface and internal heat flux, in contrast to a humid tropical climate with high solar potential. During the day and dry seasons, a three-way balance prevails between sensible heat, ground heat fluxes and net surface radiative flux, while at night and in the rainy seasons, the last two attempt to balance each other out essentially. These fluxes are around 25% greater in the dry season than in the winter.

Moorhead (2019) [81] measured evapotranspiration using a scintillometer to calculate energy fluxes in two regions in Amarillo, America. The regions studied have cold climates. The results of their work showed that the daily mean latent heat flux was between 10 W/$m^2$ and 20 W/$m^2$, and the daily mean sensible heat flux was between 5 and 15 W/$m^2$. The differences in turbulent heat fluxes between the two regions are mainly due to vapour pressure deficits.

Sensible heat flux is the energy that increases atmospheric temperature, causing advection, while latent heat corresponds to the energy available for water evaporation. This also justifies the strong increase in sensible heat flux with net radiation intensity and ambient temperature in dry seasons, compared with its low values in rainy seasons [82]. In dry seasons, radiation intensity is at a maximum, so it limits the flux of water between the components of the soil-plant-atmosphere system to reduce biological phenomena (plant transpiration and microbial respiration) ; low latent heat values are therefore obtained. As a result

of evaporation from soil surfaces due to the effects of radiant reflection in the universe, sensible heat flux and conductive heat flux are reduced in relation to sensible heat flux. In addition, latent heat intensity remained lower than that of net solar radiation. On the other hand, unexpected events are sometimes produced by major advection phenomena that cool the ambient air, minimizing the effects of net radiant fluxes and intensive biological and water exchanges. Large crops with high leaf density dampen solar radiation thermal effects more, thus minimizing net surface flux, and hence conductive and sensitive fluxes, than crops with deciduous leaves. Our results are similar to those of Su et al., (2019) [83]. According to the work of Lee et al. (2016) [68], trees perform better than grasslands in mitigating heat stress and promoting heat attenuation within the soil.

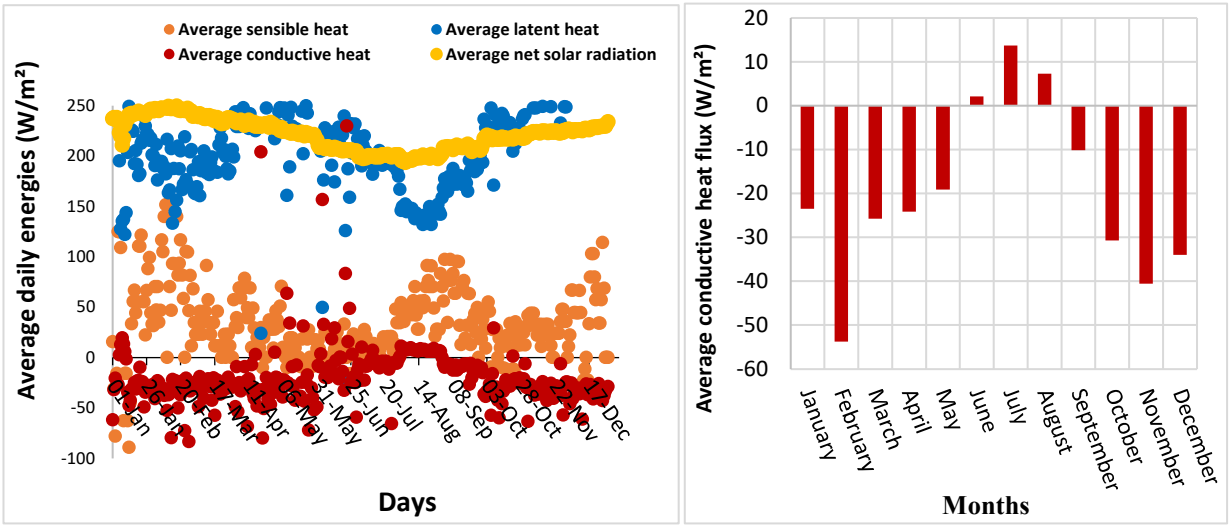


*Fig. 7. Soil energy balance: a) Heat flux from vegetation-covered soil; b) Conductive energy within the soil*

### 3.3 Relationship Between Turbulent Energy Fluxes ($Rn-G0$) And Available Energy Fluxes ($H+\lambda E$)

The study of the variation of $R_n-G_0$ as a function of $H+\lambda E$ yielded a linear regression line with a regression coefficient $R^2$ de 0,997. of 0.997. The equation for predicting the available energy flux components from the turbulent energy fluxes obtained is y = 1.008x + 17,29. The variations in $R_n-G_0$ and $H+\lambda E$ are in the range from -200 W/m² to 600 W/m² (Figure 10). These results are in line with those reported in the literature [83, 84].

Lui *et al.*, (2020) [76] studied mean diurnal variations in energy balance components at different phenological stages of rice over two years (2015–2016). The results showed that turbulent heat flux is controlled by latent heat flux, given that heat transfer phenomena are continuous processes. At night, transpiration from leaf surfaces and evaporation from soil surfaces increase ambient humidity in the absence of solar irradiation. As a result, thermal energy stored in the soil, canopy air and biomass during the day is partially released during the night. These phenomena rapidly reduce the available energy to the benefit of turbulent energy. However, during the day, the progressive increase in solar radiation intensity inevitably leads to an increase in available energy, while sensible heat is consumed by latent heat, reducing the turbulent energy flux. According to their results, if $R_n - G_0 < 0$ and LE > 0, then turbulent energy flux dominates that of available energy and vice versa. According to the results of work by Su *et al.*, (2009) [66], turbulent fluxes are strongly affected by advection, which unbalances the energy available at the ground surface by increasing evaporation from the land surface. These energy transition processes are cyclical from one day to the next and from one season to the next, and they explain the symmetrical negative and positive evolutions between available and turbulent energy fluxes. Low wind speeds, high humidity and high precipitation in the rainy seasons mean that the wetter the earth's surface, the greater the evaporation, and the more stable the atmosphere. These processes lead to reduced turbulence and atmospheric mixing. The opposite is true in the dry seasons.

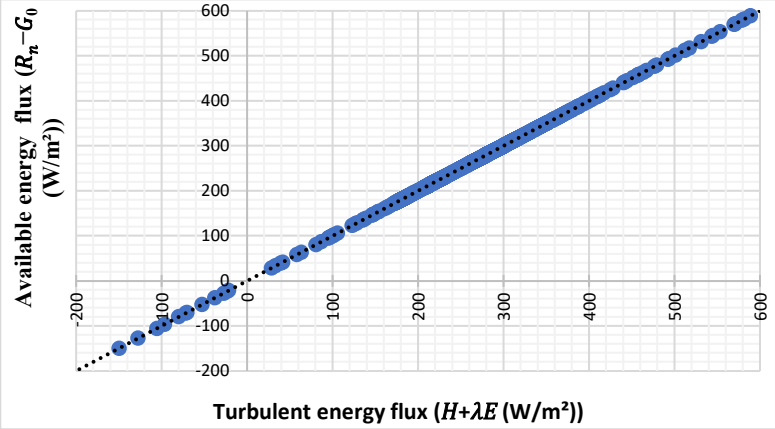


*Fig. 8. Variation of available energy ($R_n - G_0$) as a function of turbulent energy (H+ $\lambda E$)*

## 4 CONCLUSION

The present study used 11 years of meteorological data and plant biophysical properties to accurately assess conductive heat flux within croplands, under in-situ conditions. Our study used the closed-energy balance model to develop an improved version to determine daily, monthly and annual heat flux variations in the Yamoussoukro area. The results showed that rainfall in this area has been falling since 2013, increasing sensible and conductive heat fluxes. Two typical seasons were observed, including a short dry season, a long dry season, a short rainy season, and a long rainy season.

Crop growth depends on rainfall and is reduced by the dry seasons, which have a strong influence on the evolution of the leaf area index (LAI). LAI is practically constant during the long dry season, with a value of less than 2 $m^2/m^2$, and increases progressively during the rainy season, reaching a maximum of almost 6 $m^2/m^2$. Consequently, in dry seasons, latent heat fluxes are high, with rapid growth in the plant's biophysical properties. On the other hand, conductive energy quantities are high in dry seasons, ranging from -50 W/m² to 50 W/m². Excessive values in dry seasons demonstrate a demand for irrigation or the adaptation of crop types that can withstand hygrothermal changes. The water requirements of cultivated land for better plant development are felt when conductive heat has high intensities (a state of thermal stress).

This model has the advantage of being developed for all crops of interest in different zones. It can also be used in any application requiring knowledge of heat fluxes within the soil at any spatiotemporal scale.

## REFERENCES

[1] M. Kabir *et al.*, « Climate change due to increasing concentration of carbon dioxide and its impacts on environment in 21st century; a mini review », *J. King Saud Univ. - Sci.*, vol. 35, n° 5, p. 102693, juill. 2023, doi: 10.1016/j.jksus.2023.102693.

[2] E. Shahraeeni et D. Or, « Thermo-evaporative fluxes from heterogeneous porous surfaces resolved by infrared thermography », *Water Resour. Res.*, vol. 46, n° 9, p. 2009WR008455, sept. 2010, doi: 10.1029/2009WR008455.

[3] J. Ogée, E. Lamaud, Y. Brunet, P. Berbigier, et J. M. Bonnefond, « A long-term study of soil heat flux under a forest canopy », *Agric. For. Meteorol.*, vol. 106, n° 3, p. 173-186, févr. 2001, doi: 10.1016/S0168-1923 (00) 00214-8.

[4] M. M. Rahman, W. Zhang, et K. Wang, « Assessment on surface energy imbalance and energy partitioning using ground and satellite data over a semi-arid agricultural region in north China », *Agric. Water Manag.*, vol. 213, p. 245-259, mars 2019, doi: 10.1016/j.agwat.2018.10.032.

[5] Z. Xu, Y. Ma, S. Liu, W. Shi, et J. Wang, « Assessment of the Energy Balance Closure under Advective Conditions and Its Impact Using Remote Sensing Data », *J. Appl. Meteorol. Climatol.*, vol. 56, n° 1, p. 127-140, janv. 2017, doi: 10.1175/JAMC-D-16-0096.1.

[6] T. Zhang, C. Wang, S. Liu, N. Zhang, et T. Zhang, « Assessment of soil thermal conduction using artificial neural network models », *Cold Reg. Sci. Technol.*, vol. 169, p. 102907, janv. 2020, doi: 10.1016/j.coldregions.2019.102907.

[7] H. Lee, H. Mayer, et L. Chen, « Contribution of trees and grasslands to the mitigation of human heat stress in a residential district of Freiburg, Southwest Germany », *Landsc. Urban Plan.*, vol. 148, p. 37-50, avr. 2016, doi: 10.1016/j.landurbplan.2015.12.004.

[8] T. E. Link, G. N. Flerchinger, M. Unsworth, et D. Marks, « Simulation of Water and Energy Fluxes in an Old-Growth Seasonal Temperate Rain Forest Using the Simultaneous Heat and Water (SHAW) Model », *J. Hydrometeorol.*, vol. 5, nº 3, p. 443-457, juin 2004, doi: 10.1175/1525-7541 (2004) 005<0443: SOWAEF>2.0.CO; 2.

[9] Y. Ma, Z. Su, Z. Li, T. Koike, et M. Menenti, « Determination of regional net radiation and soil heat flux over a heterogeneous landscape of the Tibetan Plateau », *Hydrol. Process.*, vol. 16, nº 15, p. 2963-2971, oct. 2002, doi: 10.1002/hyp.1079.

[10] Z. Gao, X. Fan, et L. Bian, « An analytical solution to one-dimensional thermal conduction-convection in soil »:, *Soil Sci.*, vol. 168, nº 2, p. 99-107, févr. 2003, doi: 10.1097/00010694-200302000-00004.

[11] Z. Gao, « Determination of soil heat flux in a tibetan short-grass prairie », *Bound.-Layer Meteorol.*, vol. 114, nº 1, p. 165-178, janv. 2005, doi: 10.1007/s10546-004-8661-5.

[12] K. Yang et J. Wang, « A temperature prediction-correction method for estimating surface soil heat flux from soil temperature and moisture data », *Sci. China Ser. Earth Sci.*, vol. 51, nº 5, p. 721-729, mai 2008, doi: 10.1007/s11430-008-0036-1.

[13] B. G. Heusinkveld, A. F. G. Jacobs, A. A. M. Holtslag, et S. M. Berkowicz, « Surface energy balance closure in an arid region: role of soil heat flux », *Agric. For. Meteorol.*, vol. 122, nº 1-2, p. 21-37, mars 2004, doi: 10.1016/j.agrformet.2003.09.005.

[14] C. Liebethal et T. Foken, « Evaluation of six parameterization approaches for the ground heat flux », *Theor. Appl. Climatol.*, vol. 88, nº 1-2, p. 43-56, janv. 2007, doi: 10.1007/s00704-005-0234-0.

[15] A. J. Purdy, J. B. Fisher, M. L. Goulden, et J. S. Famiglietti, « Ground heat flux: An analytical review of 6 models evaluated at 88 sites and globally », *J. Geophys. Res. Biogeosciences*, vol. 121, nº 12, p. 3045-3059, déc. 2016. doi: 10.1002/2016JG003591.

[16] J. Zuo, J. Wang, J. Huang, W. Li, G. Wang, et H. Ren, « Estimation of ground heat flux and its impact on the surface energy budget for a semi-arid grassland », *Sci. Cold Arid Reg.*, 2011.

[17] D. Cava, D. Contini, A. Donateo, et P. Martano, « Analysis of short-term closure of the surface energy balance above short vegetation », *Agric. For. Meteorol.*, vol. 148, nº 1, p. 82-93, janv. 2008, doi: 10.1016/j.agrformet.2007.09.003.

[18] T. Foken, « The Energy Balance Closure Problem: An Overview », *Ecol. Appl.*, vol. 18, nº 6, p. 1351-1367, 2008.

[19] S. P. Oncley *et al.*, « The Energy Balance Experiment EBEX-2000. Part I: overview and energy balance », *Bound.-Layer Meteorol.*, vol. 123, nº 1, p. 1-28, mars 2007, doi: 10.1007/s10546-007-9161-1.

[20] L. Xing, « Analytical and numerical modeling of foundation heat exchangers », 2008.

[21] L. K. Berg et S. Zhong, « Sensitivity of MM5-Simulated Boundary Layer Characteristics to Turbulence Parameterizations », *J. Appl. Meteorol.*, vol. 44, nº 9, p. 1467-1483, sept. 2005, doi: 10.1175/JAM2292.1.

[22] M. Cuntz *et al.*, « The impact of standard and hard-coded parameters on the hydrologic fluxes in the Noah-MP land surface model », *J. Geophys. Res. Atmospheres*, vol. 121, nº 18, sept. 2016, doi: 10.1002/2016JD025097.

[23] X. Han, H. H. Franssen, C. Montzka, et H. Vereecken, « Soil moisture and soil properties estimation in the Community Land Model with synthetic brightness temperature observations », *Water Resour. Res.*, vol. 50, nº 7, p. 6081-6105, juill. 2014, doi: 10.1002/2013WR014586.

[24] T. E. Twine *et al.*, « Correcting eddy-covariance flux underestimates over a grassland », *Agric. For. Meteorol.*, vol. 103, nº 3, p. 279-300, juin 2000, doi: 10.1016/S0168-1923 (00) 00123-4.

[25] Y. Cheng *et al.*, « Failure of Taylor«s hypothesis in the atmospheric surface layer and its correction for eddy-covariance measurements », *Geophys. Res. Lett.*, vol. 44, nº 9, p. 4287-4295, mai 2017, doi: 10.1002/2017GL073499.

[26] N. Kljun, P. Calanca, M. W. Rotach, et H. P. Schmid, « A simple two-dimensional parameterisation for Flux Footprint Prediction (FFP) », *Geosci. Model Dev.*, vol. 8, nº 11, p. 3695-3713, nov. 2015, doi: 10.5194/gmd-8-3695-2015.

[27] R. Leuning, E. Van Gorsel, W. J. Massman, et P. R. Isaac, « Reflections on the surface energy imbalance problem », *Agric. For. Meteorol.*, vol. 156, p. 65-74, avr. 2012, doi: 10.1016/j.agrformet.2011.12.002.

[28] H.-D. Wizemann, J. Ingwersen, P. Högy, K. Warrach-Sagi, T. Streck, et V. Wulfmeyer, « Three year observations of water vapor and energy fluxes over agricultural crops in two regional climates of Southwest Germany », *Meteorol. Z.*, vol. 24, nº 1, p. 39-59, mars 2015, doi: 10.1127/metz/2014/0618.

[29] J. Vanderborght, T. Fetzer, K. Mosthaf, K. M. Smits, et R. Helmig, « Heat and water transport in soils and across the soil-atmosphere interface: 1. Theory and different model concepts », *Water Resour. Res.*, vol. 53, nº 2, p. 1057-1079, févr. 2017, doi: 10.1002/2016WR019982.

[30] H.-D. Wizemann, J. Ingwersen, P. Högy, K. Warrach-Sagi, T. Streck, et V. Wulfmeyer, « Three year observations of water vapor and energy fluxes over agricultural crops in two regional climates of Southwest Germany », *Meteorol. Z.*, vol. 24, nº 1, p. 39-59, mars 2015, doi: 10.1127/metz/2014/0618.

[31] K. H. J. Kokobou, A. B. Konan-Waidhet, T. D. Soro, et J. Biemi, « Mapping of Potential Recharge Areas of Fractured Aquifers in the Departments of Yamoussoukro and Toumodi (Central Côte d'Ivoire) », *J. Geogr. Inf. Syst.*, vol. 14, nº 05, p. 527-545, 2022, doi: 10.4236/jgis.2022.145030.

[32] K. H. J. Kokobou, A. B. Konan-Waidhet, T. D. Soro, et J. Biemi, « Mapping of Potential Recharge Areas of Fractured Aquifers in the Departments of Yamoussoukro and Toumodi (Central Côte d'Ivoire) », *J. Geogr. Inf. Syst.*, vol. 14, n° 05, p. 527-545, 2022, doi: 10.4236/jgis.2022.145030.

[33] A. Guillaume, K.-W. Arthur Brice, S. A. Parfait, K. K. Hervé Jacques, et B. Jea, « Landsat 8 oli Satellite Imagery Mapping and Analysis of Bedrock Fracture Networks in the Departments of Yamoussoukro and Toumodi (Central Cote d«Ivoire) », *Eur. Sci. J. ESJ*, vol. 18, n° 30, p. 206, sept. 2022, doi: 10.19044/esj.2022.v18n30p206.

[34] K. M. Ehoussou et A. M. Kouassi, « Caractérisation hydrogéochimique des aquifères fissurés de la région du bélier, centre de la Côte D«Ivoire », 2019.

[35] A. A. Guillaume, K.-W. A. Brice, S. A. Parfait, K. K. H. Jacques, et B. Jean, « Landsat 8 Oli Satellite Imagery Mapping and Analysis of Bedrock Fracture Networks in the Departments of Yamoussoukro and Toumodi (Central Cote d«Ivoire) », *Eur. Sci. J. ESJ*, vol. 8, sept. 2022, doi: 10.19044/esipreprint.8.2022.p391.

[36] A. Kniffka, P. Knippertz, et A. H. Fink, « The role of low-level clouds in the West African monsoon system », *Atmospheric Chem. Phys.*, vol. 19, n° 3, p. 1623-1647, févr. 2019, doi: 10.5194/acp-19-1623-2019.

[37] O. O. Apeh, O. K. Overen, et E. L. Meyer, « Monthly, Seasonal and Yearly Assessments of Global Solar Radiation, Clearness Index and Diffuse Fractions in Alice, South Africa », *Sustainability*, vol. 13, n° 4, p. 2135, févr. 2021. doi: 10.3390/su13042135.

[38] W. P. Kustas, C. S. T. Daughtry, et P. J. Van Oevelen, « Analytical treatment of the relationships between soil heat flux/net radiation ratio and vegetation indices », *Remote Sens. Environ.*, vol. 46, n° 3, p. 319-330, déc. 1993, doi: 10.1016/0034-4257 (93) 90052-Y.

[39] T. Allmendinger, « The Thermal Radiation of the Atmosphere and Its Role in the So-Called Greenhouse Effect », *Atmospheric Clim. Sci.*, vol. 08, n° 02, p. 212-234, 2018, doi: 10.4236/acs.2018.82014.

[40] K. Wilson *et al.*, « Energy balance closure at FLUXNET sites », *Agric. For. Meteorol.*, vol. 113, n° 1-4, p. 223-243, déc. 2002, doi: 10.1016/S0168-1923 (02) 00109-0.

[41] A. G. Barr, K. Morgenstern, T. A. Black, J. H. McCaughey, et Z. Nesic, « Surface energy balance closure by the eddy-covariance method above three boreal forest stands and implications for the measurement of the CO2 flux », *Agric. For. Meteorol.*, vol. 140, n° 1-4, p. 322-337, nov. 2006, doi: 10.1016/j.agrformet.2006.08.007.

[42] N. R. Nelli *et al.*, « Micrometeorological measurements in an arid environment: Diurnal characteristics and surface energy balance closure », *Atmospheric Res.*, vol. 234, p. 104745, avr. 2020, doi: 10.1016/j.atmosres.2019.104745.

[43] M. M. S. El-Din, « On the heat flow into the ground », *Renew. Energy*, 1999.

[44] M. Menenti et B. J. Choudhury, « Parameterization of land surface evaporation by means of location dependent potential evaporation and surface temperature range », *IAHS Publ. no. 212*, 1993.

[45] C. Zhan, « Quantitative estimation of land surface evapotranspiration in Taiwan based on MODIS data », vol. 4, n° 3, 2011.

[46] G. Van Durme et M. Erpicum, « Variabillité spatio-temporelle de l'albédo. analyse menée à la résolution métrique », 2005, *Bulletin de la Société géographique de Liège*.

[47] A. Vidal, *Estimation de l'évapotranspiration par télédétection: application au contrôle de l'irrigation*. Antony, France: Cemagref-Dicova, 1990. Consulté le: 2 mai 2020. [En ligne]. Disponible sur: http://public.ebookcentral.proquest.com/choice/publicfullrecord.aspx?p=3399040.

[48] A. Allahem, S. Boulaaras, K. Zennir, et M. Haiour, « A new mathematical model of heat equations and its application on the agriculture soil », p. 28, 2018.

[49] V. Bourdin, « Calculs astronomiques simplifiés », p. 10, 2014.

[50] J. Zhao *et al.*, « Estimating fractional vegetation cover from leaf area index and clumping index based on the gap probability theory », *Int. J. Appl. Earth Obs. Geoinformation*, vol. 90, p. 102112, août 2020, doi: 10.1016/j.jag.2020.102112.

[51] W. Zhuo, H. Huang, X. Gao, X. Li, et J. Huang, « An Improved Approach of Winter Wheat Yield Estimation by Jointly Assimilating Remotely Sensed Leaf Area Index and Soil Moisture into the WOFOST Model », *Remote Sens.*, vol. 15, n° 7, p. 1825, mars 2023, doi: 10.3390/rs15071825.

[52] J. Liu *et al.*, « Validation of Moderate Resolution Imaging Spectroradiometer (MODIS) albedo retrieval algorithm: Dependence of albedo on solar zenith angle », *J. Geophys. Res. Atmospheres*, vol. 114, n° D1, p. 2008JD009969, janv. 2009, doi: 10.1029/2008JD009969.

[53] G. Nizinski, G. Galat, et A. Galat-Luong, « Etude et modélisation de l'évapotranspiration des couverts végétaux : cas d'une savane et d'une plantation », 2010.

[54] J. J. Nizinski, G. Galat, A. Galat-Luong, M. Dingkuhn, et D. Fabre, « Evapotranspiration réelle et résistance du couvert d'une savane à *Loudetia arundinacea* (bassin du Kouilou, Congo-Brazzaville) », *Climatologie*, vol. 6, p. 33-45, 2009, doi: 10.4267/climatologie.460.

[55] Z. Su, « The Surface Energy Balance System (SEBS) for estimation of turbulent heat fluxes », *Hydrol. Earth Syst. Sci.*, vol. 6, n° 1, p. 85-100, 2002, doi: 10.5194/hess-6-85-2002.

[56] Hamimed Abderrahmane, Abdelkader Khaldi, et Zaagane Mansour, « Méthodologie d'estimation de l»évapotranspiration et des flux énergétiques de surface à partir des données satellitaires thermiques et des modèles du bilan énergétique. », 2018, doi: 10.13140/RG.2.2.20407.98727/2.

[57] Y. Su *et al.*, « Quantifying the biophysical effects of forests on local air temperature using a novel three-layered land surface energy balance model », *Environ. Int.*, vol. 132, p. 105080, nov. 2019, doi: 10.1016/j.envint.2019.105080.

[58] B. A. Hssaine *et al.*, « Calibrating an evapotranspiration model using radiometric surface temperature, vegetation cover fraction and near-surface soil moisture data », *Agric. For. Meteorol.*, vol. 256-257, p. 104-115, juin 2018, doi: 10.1016/j.agrformet.2018.02.033.

[59] J. C. B. Hoedjes, A. Chehbouni, F. Jacob, J. Ezzahar, et G. Boulet, « Deriving daily evapotranspiration from remotely sensed instantaneous evaporative fraction over olive orchard in semi-arid Morocco », *J. Hydrol.*, vol. 354, nº 1-4, p. 53-64, juin 2008, doi: 10.1016/j.jhydrol.2008.02.016.

[60] J. J. Nizinski, G. Galat, A. Galat-Luong, M. Dingkuhn, et D. Fabre, « Evapotranspiration réelle et résistance du couvert d'une savane à loudetia arundinacea (bassin du Kouilou, Congo-Brazzaville) », *Climatologie*, nº Volume 6, 2009, doi: 10.4267/climatologie.460.

[61] G. Nizinski, G. Galat, et A. Galat-Luong, « Etude et modélisation de l'évapotranspiration des couverts végétaux : cas d'une savane et d'une plantation », p. 6, 2010.

[62] J. A. Businger, « Introduction to Obukhov's paper on »turbulence in an atmosphere with a non-uniform temperature« ».

[63] U. Silins et R. L. Rothwell, « Forest Peatland Drainage and Subsidence Affect Soil Water Retention and Transport Properties in an Alberta Peatland », *Soil Sci. Soc. Am. J.*, vol. 62, nº 4, p. 1048-1056, juill. 1998. doi: 10.2136/sssaj1998.03615995006200040028x.

[64] W. J. Massman, « A model study of kBHΧ1 for vegetated surfaces using localized near- field Lagrangian theory », *J. Hydrol.*, p. 17, 1999.

[65] J. Hao et E. Lu, « Variation of Relative Humidity as Seen through Linking Water Vapor to Air Temperature: An Assessment of Interannual Variations in the Near-Surface Atmosphere », *Atmosphere*, vol. 13, nº 8, p. 1171, juill. 2022, doi: 10.3390/atmos13081171.

[66] Z. (Bob) Su, « ESA Advanced training course on remote sensing SEBS - Surface Energy Balance System for estimation of turbulent heat fluxes and evapotranspiration », 2009, *International Institute for Geo-Information Science and Earth Observation (ITC), Enschede, The Netherlands B_SU@ITC.NL, www.itc.nl/wrs*.

[67] J. Wu, S. Zhang, H. Wu, S. Liu, Y. Qin, et J. Qin, « Actual Evapotranspiration in Suli Alpine Meadow in Northeastern Edge of Qinghai-Tibet Plateau, China », *Adv. Meteorol.*, vol. 2015, p. 1-10, 2015, doi: 10.1155/2015/593649.

[68] B. Silva Oliveira, E. Caria Moraes, M. Carrasco-Benavides, G. Bertani, et G. Augusto Verola Mataveli, « Improved Albedo Estimates Implemented in the METRIC Model for Modeling Energy Balance Fluxes and Evapotranspiration over Agricultural and Natural Areas in the Brazilian Cerrado », *Remote Sens.*, vol. 10, nº 8, p. 1181, juill. 2018, doi: 10.3390/rs10081181.

[69] J. W. Taylor *et al.*, « Aerosol influences on low-level clouds in the West African monsoon », *Atmospheric Chem. Phys.*, vol. 19, nº 13, p. 8503-8522, juill. 2019, doi: 10.5194/acp-19-8503-2019.

[70] G. Pante, P. Knippertz, A. H. Fink, et A. Kniffka, « The potential of increasing man-made air pollution to reduce rainfall over southern West Africa », *Atmospheric Chem. Phys.*, vol. 21, nº 1, p. 35-55, janv. 2021, doi: 10.5194/acp-21-35-2021.

[71] M. Maranan, A. H. Fink, et P. Knippertz, « Rainfall types over southern West Africa: Objective identification, climatology and synoptic environment », *Q. J. R. Meteorol. Soc.*, vol. 144, nº 714, p. 1628-1648, juill. 2018, doi: 10.1002/qj.3345.

[72] S. P. C. Yeboua, Y. N«Goran, et K. Konan, « Classification of Hourly Clearness Index of Solar Radiation in the District of Yamoussoukro », *Energy Power Eng.*, vol. 11, nº 05, p. 220-231, 2019, doi: 10.4236/epe.2019.115014.

[73] T. R. Ayodele et A. S. O. Ogunjuyigbe, « Prediction of monthly average global solar radiation based on statistical distribution of clearness index », *Energy*, vol. 90, p. 1733-1742, oct. 2015, doi: 10.1016/j.energy.2015.06.137.

[74] J. Moorhead *et al.*, « Evaluation of Sensible Heat Flux and Evapotranspiration Estimates Using a Surface Layer Scintillometer and a Large Weighing Lysimeter », *Sensors*, vol. 17, nº 10, p. 2350, oct. 2017, doi: 10.3390/s17102350.

[75] S. Goswami, J. Gamon, S. Vargas, et C. Tweedie, « Relationships of NDVI, Biomass, and Leaf Area Index (LAI) for six key plant species in Barrow, Alaska », PeerJ PrePrints, preprint, mars 2015. doi: 10.7287/peerj.preprints.913v1.

[76] X. Liu, J. Xu, X. Zhou, W. Wang, et S. Yang, « Evaporative fraction and its application in estimating daily evapotranspiration of water-saving irrigated rice field », *J. Hydrol.*, vol. 584, p. 124317, mai 2020, doi: 10.1016/j.jhydrol.2019.124317.

[77] J. Timmermans, Z. Su, C. Van Der Tol, A. Verhoef, et W. Verhoef, « Quantifying the uncertainty in estimates of surface–atmosphere fluxes through joint evaluation of the SEBS and SCOPE models », *Hydrol. Earth Syst. Sci.*, vol. 17, nº 4, p. 1561-1573, avr. 2013, doi: 10.5194/hess-17-1561-2013.

[78] J. L. Chávez, C. M. U. Neale, J. H. Prueger, et W. P. Kustas, « Daily evapotranspiration estimates from extrapolating instantaneous airborne remote sensing ET values », *Irrig. Sci.*, vol. 27, n° 1, p. 67-81, nov. 2008, doi: 10.1007/s00271-008-0122-3.

[79] T. Fetzer, J. Vanderborght, K. Mosthaf, K. M. Smits, et R. Helmig, « Heat and water transport in soils and across the soil-atmosphere interface: 2. Numerical analysis », *Water Resour. Res.*, vol. 53, n° 2, p. 1080-1100, févr. 2017, doi: 10.1002/2016WR019983.

[80] D. P. Ariyanto, Z. A. Qudsi, Sumani, W. S. Dewi, Rahayu, et Komariah, « The dynamic effect of air temperature and air humidity toward soil temperature in various lands cover at KHDTK Gunung Bromo, Karanganyar - Indonesia », *IOP Conf. Ser. Earth Environ. Sci.*, vol. 724, n° 1, p. 012003, avr. 2021, doi: 10.1088/1755-1315/724/1/012003.

[81] J. E. Moorhead, « Field-Scale Estimation of Evapotranspiration », in *Advanced Evapotranspiration Methods and Applications*, D. Bucur, Éd., IntechOpen, 2019. doi: 10.5772/intechopen.80945.

[82] M. M. Rahman, W. Zhang, et K. Wang, « Assessment on surface energy imbalance and energy partitioning using ground and satellite data over a semi-arid agricultural region in north China », *Agric. Water Manag.*, vol. 213, p. 245-259, mars 2019, doi: 10.1016/j.agwat.2018.10.032.

[83] Y. Su *et al.*, « Quantifying the biophysical effects of forests on local air temperature using a novel three-layered land surface energy balance model », *Environ. Int.*, vol. 132, p. 105080, nov. 2019, doi: 10.1016/j.envint.2019.105080.

[84] V. Raman, M. Kumar, A. Sharma, D. Froehlich, et A. Matzarakis, « Quantification of thermal stress abatement by trees, its dependence on morphology and wind: A case study at Patna, Bihar, India », *Urban For. Urban Green.*, vol. 63, p. 127213, août 2021, doi: 10.1016/j.ufug.2021.127213.

[85] A. M. D. R. F. Jardim *et al.*, « Monitoring Energy Balance, Turbulent Flux Partitioning, Evapotranspiration and Biophysical Parameters of Nopalea cochenillifera (Cactaceae) in the Brazilian Semi-Arid Environment », *Plants*, vol. 12, n° 13, p. 2562, juill. 2023, doi: 10.3390/plants12132562.

[86] A. Abdolghafoorian et L. Farhadi, « Estimation of Surface Turbulent Fluxes From Land Surface Moisture and Temperature Via a Variational Data Assimilation Framework », *Water Resour. Res.*, vol. 55, n° 6, p. 4648-4667, juin 2019, doi: 10.1029/2018WR024580.